Applied Catalysis B: Environment and Energy 363 (2025) 124831

Contents lists available at ScienceDirect

Applied Catalysis B: Environment and Energy

journal homepage: www.elsevier.com/locate/apcatb

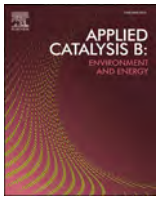

A $MoNi_4$(312) surface preferred reconstruction enhancing hydrogen evolution

Song Xie [a,1], Chao Huang [b,1], Hao Dong [a], Baochai Xu [a], Yaping Miao [c], Biao Gao [d], Xuming Zhang [d], Paul K. Chu [b], Xiang Peng [a,*]

[a] Hubei Key Laboratory of Plasma Chemistry and Advanced Materials, Engineering Research Center of Phosphorus Resources Development and Utilization of Ministry of Education, School of Materials Science and Engineering, Wuhan Institute of Technology, Wuhan 430205, China
[b] Department of Physics, Department of Materials Science and Engineering, and Department of Biomedical Engineering, City University of Hong Kong, Tat Chee Avenue, Kowloon, Hong Kong
[c] School of Textile Science and Engineering, Xi'an Polytechnic University, Xi'an 710048, China
[d] The State Key Laboratory of Refractories and Metallurgy, Institute of Advanced Materials and Nanotechnology, Wuhan University of Science and Technology, Wuhan 430081, China

ARTICLE INFO

Keywords:
NiMo alloy
Hydrogen evolution reaction
Electrocatalytic water splitting
Surface reconstruction
Crystal facet orientation

ABSTRACT

Nickel-molybdenum (Ni-Mo) alloys have garnered significant attention for superior electrocatalytic hydrogen evolution reaction (HER). Generally, catalysts undergo reconstruction during HER, leading to surface structure evolution, which is crucial for catalytic properties. However, the real electroactive sites and mechanisms underlying the structure evolution of Ni-Mo alloys through the electrochemical process remain unclear. Herein, we propose a Ni-Mo alloy with enriched $MoNi_4$(312) plane exposure after electrochemical reconstruction due to its preferential growth during the HER. The atomic interaction within the $MoNi_4$(312) plane facilitates the electron transfer from Ni to Mo and optimizes the electronic configuration, accelerating the release of gaseous hydrogen and smoothing the HER process. The reconstructed Ni-Mo alloy demonstrates exceptional HER performance, achieving an ultrasmall overpotential of 23 mV at 10 mA cm^{-2}. Additionally, by scaling up the electrode by 8 times, the overpotentials required remain similar to a small electrode. This study provides insights into surface reconstruction and orientational crystal plane design of low-cost transition metal-based alloy catalysts for industrial hydrogen production.

1. Introduction

The global energy transition toward sustainable and clean alternatives has propelled hydrogen energy as a promising candidate to replace fossil fuels [1–3]. Owing to its high energy density and environmentally friendly characteristics, hydrogen offers a viable solution to the current energy and environmental crises [4–6]. Hydrogen production *via* the hydrogen evolution reaction (HER) in electrocatalytic water splitting, powered by renewable sources, is the key to achieving zero-carbon-emission energy [7–9]. However, the high cost and scarce availability of noble metals like Pt and Pd, which are often used as HER catalysts, present a significant hurdle for large-scale commercialization [10,11]. As a result, there is an acute need to develop innovative and cost-effective catalysts to realize sustainable and economical hydrogen production.

Alloy materials consisting of various metal elements are beneficial in adjusting the electronic structure and surface properties of the catalyst [12]. The synergistic effect between metal elements optimizes the reaction path and reduces energy barriers [13–15]. Therefore, alloy catalysts show great potential in the field of electrocatalysis and have attracted widespread interest [16]. In particular, nickel-molybdenum (Ni-Mo) alloys exhibit impressive HER catalytic activity, making it a promising alternative to Pt-group catalysts and a subject of extensive exploration [17]. For instance, Wang *et al.* [18] have prepared $MoNi_4$ nanoparticles by reducing doped molybdenum salts on $Ni(OH)_2$ nanosheets. The resulting catalyst has good properties in HER, such as an overpotential of 56 mV to attain a current density of 10 mA cm^{-2}. Nairan *et al.* [19] have fabricated NiMo solid solution alloy with good HER

* Corresponding author.
E-mail address: xpeng@wit.edu.cn (X. Peng).
[1] These authors contributed equally to this work.

https://doi.org/10.1016/j.apcatb.2024.124831
Received 25 September 2024; Received in revised form 8 November 2024; Accepted 16 November 2024
Available online 17 November 2024

activity and stability. A low overpotential of 17 mV is enough to drive a current density of 10 mA cm^{-2}. The exceptional properties may be attributed to the incorporation of Mo dopants, which form the alloy and generate abundant $MoNi_4$ active sites, while simultaneously inducing lattice distortion to create highly active interfaces. Generally, the structure-performance relationships of Ni-Mo-based catalysts are based on their initial structures before the catalytic reactions. However, the surface of a catalyst undergoes structure evolution during the HER, originating from both the chemical etching by the electrolyte and electrochemical reduction by the electric field [17,20]. This leads to inaccuracies in the structure-performance relationships based on the initial structure and the observed catalytic performance. Therefore, uncovering the surface structure evolution of alloys during HER is crucial for elucidating their electrocatalytic mechanism. Nevertheless, there is still a lack of in-depth research and insights into the surface reconstruction and activity origins of Ni-Mo alloy catalysts during HER.

Herein, we proposed a Ni-Mo alloy with specific crystal plane exposure through electrochemical reconstruction for superior HER, as illustrated in Scheme 1. By conducting thorough theoretical analysis and experiments, we elucidate the mechanism underlying the oriented growth of the $MoNi_4$(312) crystal plane during the electrochemical reconstruction process. The chemically dissolved Ni^{2+} and MoO_4^{2-} near the cathode adsorbed to $MoNi_4$(312) surface, which is more favorable for Ni^{2+} adsorption, thus promoting its orientational growth. Furthermore, the interaction between Ni and Mo atoms on the $MoNi_4$(312) crystal plane weakens the extremely strong hydrogen adsorption capability, resulting in enhanced HER catalytic activity. Consequently, the $MoNi_4$ alloy with the substantially exposed (312) crystal plane achieves an impressive overpotential of only 23 mV for a current density of 10 mA cm^{-2} as well as stable operation for 100 h at 100 mA cm^{-2}. More importantly, the enlarged $MoNi_4$ electrode with 8 times larger geometrical size prepared through the scale-up protocol achieved a current of 1 A (approximately 111 mA cm^{-2}) at a small overpotential of 91 mV in HER, demonstrating promising industrial application.

2. Experiment details

2.1. Materials preparation

5.00 g of nickel sulfate hexahydrate ($NiSO_4{\cdot}6\ H_2O$), 0.40–1.00 g of sodium molybdate dihydrate ($Na_2MoO_4{\cdot}2\ H_2O$), 8.00 g of sodium citrate ($Na_3C_6H_5O_7$), 0.02 g of sodium dodecyl sulfate, 0.16 g of saccharin ($C_7H_5NO_3S$), and 0.016 g of 1,4-butanediol ($C_4H_6O_2$) were dissolved in 100 mL of deionized water (DW). Ammonium hydroxide was added to adjust the pH, followed by heating to 35 ℃. Subsequently, a two-electrode cell composed of a cleaned stainless steel (SS) plate as the cathode and a graphite rod as the anode was immersed in the electroplating solution and driven by a direct-current power supply (IT6332L, ITECH ELECTRONIC Co., Ltd.). The current density was set at 30 mA cm^{-2} with an electroplating duration of 3 h. Afterwards, the SS plate was rinsed with DW and dried in air. The products were denoted as NM4, NM6, NM8, and NM10, where the numbers represent the concentration of $Na_2MoO_4{\cdot}2\ H_2O$ added, which were 4, 6, 8, and 10 g L^{-1}, respectively.

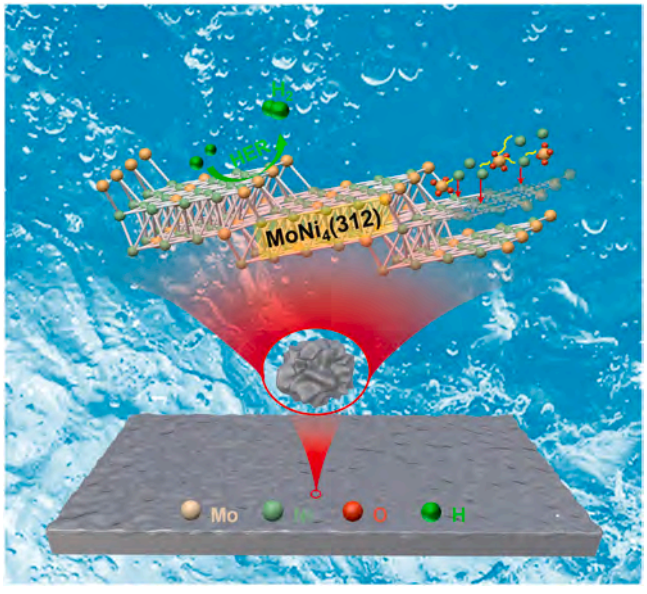

Scheme 1. Schematic illustration of *in situ* reconstruction and enhanced HER on the $MoNi_4$(312) crystal plane.

2.2. Materials characterization

The morphology and composition of the samples were characterized by scanning electron microscopy (FE-SEM, TESCAN MIRA4) and energy-dispersive X-ray spectroscopy (EDS). The crystal structure was determined by X-ray diffraction (XRD, LabX XRD-6100, Shimadzu) with a Cu K_α source. The Raman scattering (HR RamLab) was conducted to reveal the surface evolution during the electrochemical process. X-ray photoelectron spectroscopy (XPS, Thermo Scientific *K*-Alpha, Thermo Fisher) with monochromatic Al K_α X-ray was conducted to determine the surface composition and chemical states. The electrical conductivity of the samples was measured by Van der Pauw's four-point probe method using the Keithley 2450.

2.3. Electrochemical measurement

The electrochemical measurements were performed using a three-electrode configuration on the CHI 760E electrochemical workstation (Shanghai CH Instrument, China). A modified SS, saturated calomel electrode (SCE), and graphite rod served as the working electrode, reference electrode, and counter electrode, respectively. All the potentials were referenced to the reversible hydrogen electrode (RHE) based on the Nernst equation: $E_{RHE} = E_{SCE} + 0.242 + 0.059 \times pH$. The pH of the 0.5 M H_2SO_4 electrolyte was measured to be 0.58 by a pH meter (FE28, Mettler Toledo). Linear sweep voltammetry (LSV) was conducted at a scanning rate of 10 mV s^{-1} with *iR*-compensation. The Tafel slope was calculated by the formula $\eta = a + b\log(|j|)$, where η represents overpotential, j denotes current density, a is a constant, and b is the Tafel slope. Nyquist plots were carried out at the initial potential of –0.33 V *vs.* SCE in the frequency range of 100 kHz to 1 Hz with an amplitude of 5 mV. The electrochemically active surface area (ECSA) was determined by cyclic voltammetry (CV) at scanning rates of 1-10 mV s^{-1} in the potential window between –0.20 and –0.16 V *vs.* SCE. The stability was assessed at a constant current density of 0.1 A cm^{-2} for 100 h. The quantities of H_2 produced were determined by the water displacement method.

2.4. DFT calculations

The density-functional theory (DFT) calculation was implemented in the Vienna ab initio simulation package (VASP) [21] *via* the first principle plane-wave pseudopotential formation and generalized gradient approximation (GGA) of the Perdew-Burke-Ernzerhof (PBE) function. The binding energies of the $MoNi_4$(312) and $MoNi_4$(121) surfaces with extra Ni are:

$$\Delta E_{Ni(312)} = E_{Ni\text{-}Ni(312)} - E_{Ni+Ni(312)} \quad (1)$$

$$\Delta E_{Ni(121)} = E_{Ni\text{-}Ni(121)} - E_{Ni+Ni(121)} \quad (2)$$

where $E_{Ni+Ni(312)}$ represents the total energy of the bulk metal of $MoNi_4$(312) and the isolated Ni atom before the Ni absorption and $\Delta E_{Ni\text{-}Ni(312)}$ represents the total energy of the bulk metal of $MoNi_4$(312) and

the absorbed Ni atom after Ni absorption and the same as the $MoNi_4$(121). The calculation of Ni stripping off the $MoNi_4$ cathode surface is similar. In the structure optimization, a 400.0 eV cutoff energy, 10^{-5} eV energy convergence accuracy, 0.03 eV $Å^{-1}$ residual force, and 2 × 3 × 1 k-mesh for (312) and (121) are used. In the calculation of the free energy for adsorbed hydrogen (ΔG_{H^*}), a 450.0 eV cutoff energy and 0.02 eV $Å^{-1}$ residual force are applied. ΔG_{H^*} [22] is calculated as follows:

$$\Delta G_{H^*} = \Delta E + \Delta(\mathrm{ZPE}) - T\Delta S \quad (3)$$

$$\Delta E = E_{(\mathrm{surface+H})} - E_{(\mathrm{surface})} - 1/2\, E_{(\mathrm{H2})} \quad (4)$$

where ΔS is the entropy, $E_{(\mathrm{surface\ +\ H})}$ is the total energy of the system with the H-adatom bound to the basal plane, $E_{(\mathrm{surface})}$ is the total energy of the pristine system, $E_{(\mathrm{H2})}$ is the total energy of the H_2 molecule, and Δ(ZPE) is the difference between the zero-point energy (ZPE) of the H-adatom and the ZPE of the H_2 molecule calculated by the normal mode analysis. The entropy of molecular hydrogen in the gas phase is under standard conditions (1 bar of H_2, pH = 0, and temperature T = 298.15 K).

3. Results and discussion

3.1. Catalyst characterization

Fig. 1a shows the co-deposition of nickel and molybdenum under constant current conditions and the formation of the Ni-Mo alloy coating. The application of a constant current density of 30 mA cm^{-2} in the electrolytic cell prompts the Ni^{2+} ions to migrate toward the cathodic SS substrate, thus generating an electric layer of positive Ni^{2+} ions on the surface. Simultaneously, MoO_4^{2-} ions in the electrolyte adsorb onto the positively charged layer and are electrochemically reduced together with nickel ions, forming a Ni-Mo alloy coating on the SS surface. A series of Ni-Mo alloys (NM4, NM6, NM8, and NM10) were prepared by adjusting the concentration of $Na_2MoO_4{\cdot}2\ H_2O$ source (4, 6, 8, 10 g L^{-1}) in the electroplating solution. XRD is employed to determine the composition and structure of the products, as shown in Fig. S1. Electroplating using the initial plating solution without the addition of $Na_2MoO_4{\cdot}2\ H_2O$ results in the deposition of metallic Ni (JCPDS card No. 04–0850). The sample of NM4 is a coating composed of the (121) single crystal plane of $MoNi_4$ (JCPDS card No. 65–5480), while the crystal phases of NM6, NM8, and NM10 are similar, with variations only in the intensity of the diffraction peak at 74.7°, which corresponds to the $MoNi_4$(312) plane. As shown in Fig. 1b, peak fitting analysis of the XRD

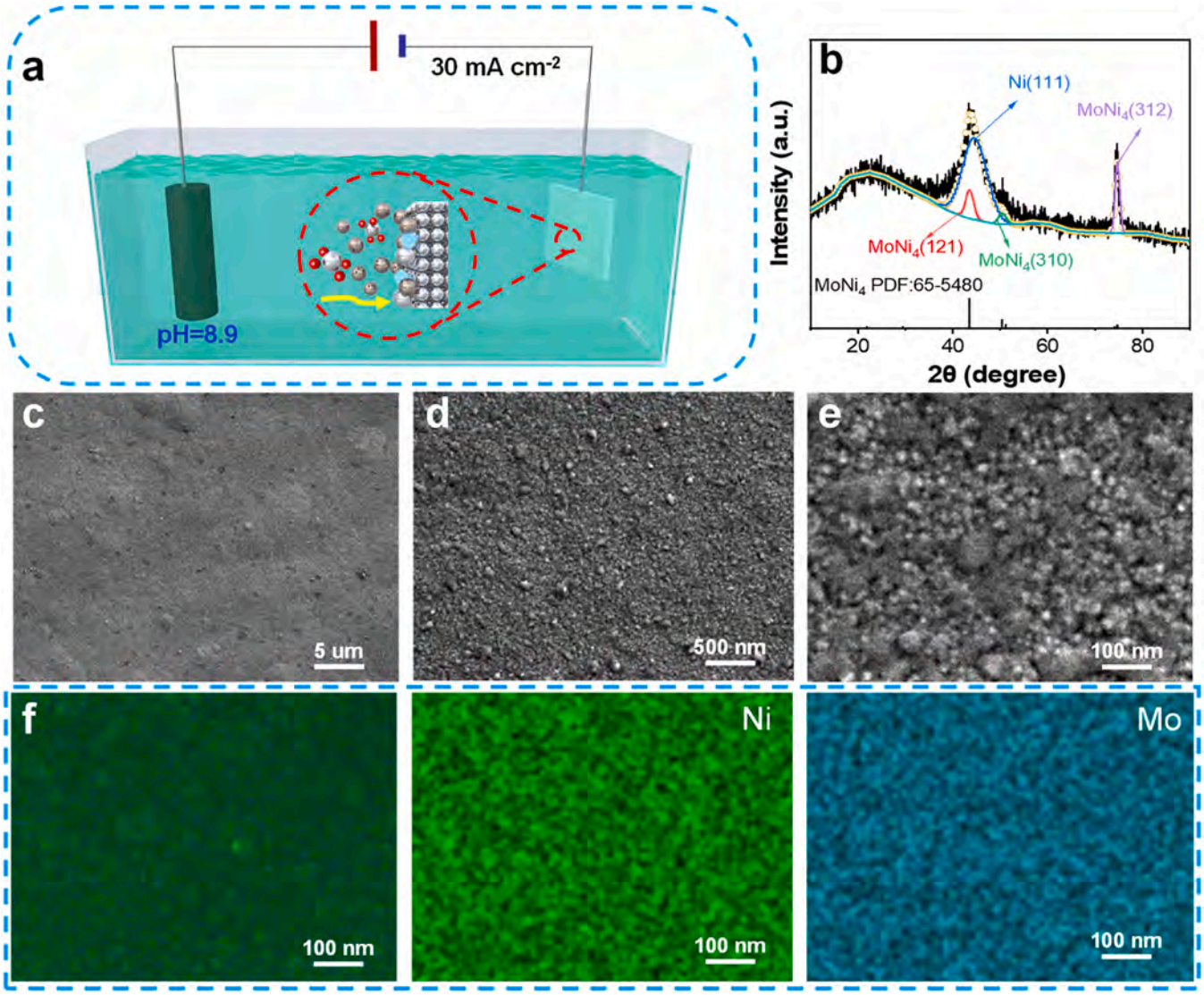

Fig. 1. (a) Schematic diagram of the synthesis of $NiMo_4$; (b) XRD pattern, (c-e) FE-SEM images, and (f) Elemental maps of Mo and Ni of NM8.

pattern of NM8 revealed a broad diffraction peak at 44.5° corresponding to the Ni(111) crystal plane [23,24], while the peaks at 43.5°, 51.2°, and 74.7° correspond to the (121), (310), and (312) crystal planes of $MoNi_4$, respectively. Notably, compared to the standard PDF card, the initial NM8 prepared by electrodeposition exhibits a higher intensity for the diffraction peak at 74.7°, corresponding to the $MoNi_4$(312) plane. This may be attributed to the orientated growth of this crystal plane during electroplating [25]. The electronic structures and electrocatalytic activities vary with crystal planes, therefore the preferential growth of a specific plane may play a significant role in HER performance.

The FE-SEM images in Figs. S2 and 1c-e reveal that the coatings are composed of nanoparticles. EDS shows that Ni and Mo are distributed uniformly in NM8, as shown in Fig. 1f. The atomic concentrations of Ni and Mo in NM8 are determined to be 76.48 % and 23.52 %, respectively, as shown in Fig. S3. Fig. S4a shows the lustrous surface of NM8. Cross-sectional observations of NM8 were conducted using FE-SEM (Fig. S4b-c), revealing a total thickness of the NM8 sample of 92 μm, with the thickness of Ni-Mo alloy coating of 8 μm at both sides. The electrical conductivity of NM8 is measured to be 1.22×10^4 S cm^{-1}, which is comparable to that of the conductive SS substrate, as shown in Fig. S5. Fig. S6 demonstrates the assembling of Ni-Mo alloy coating on SS of the as-prepared NM8, showing a layer of Ni-Mo alloy on the surface of SS with high conductivity. The exceptional conductivity promotes electron transfer in the electrochemical reactions [26,27].

3.2. Electrochemical reconstruction

Comprehensive characterization provided a detailed understanding of the initial structure of the catalysts. Electrochemical measurements were conducted on NM8. The dynamic changes in its structure and catalytic performance during the electrochemical process were monitored to establish a real structure-electrocatalytic activity relationship. All the potentials in LSV curves are *iR* corrected to evaluate the intrinsic activity of the catalysts in HER. Fig. S7 shows the initial 100 LSV curves of NM8 in 0.5 M H_2SO_4, revealing a gradual enhancement in the electrochemical performance as the scans progress. The overpotential of NM8 at 10 mA cm^{-2} during 100 consecutive LSV scans is shown in Fig. 2a. With the number of scans increasing, the overpotential decreases steadily from the initial value of 78 mV, stabilizes around the 80th scan, and reaches 23 mV by the 100th scan. Similarly, the overpotential decreases from 218 mV to 78 mV for a current density of 100 mA cm^{-2}. The *in situ* Nyquist plots results in Fig. S8 reveal that the charge transfer resistance (R_{ct}) of NM8 diminishes rapidly and eventually stabilizes at about the 80th scan. The decrease in R_{ct} during the initial scans signifies the accelerated kinetics of NM8 in HER. The HER activity depends on the ECSA of the catalyst, which can be expressed by the electrical double-layer capacitance (C_{dl}) in the non-Faradic regions based on the CV curves, as shown in Fig. S9. Fig. S10 shows that the C_{dl} of NM8 after the initial 100 cycles of LSV scanning is 331 mF cm^{-2}, which is twice as large as the initial value (161 mF cm^{-2}). A larger ECSA results in enhanced

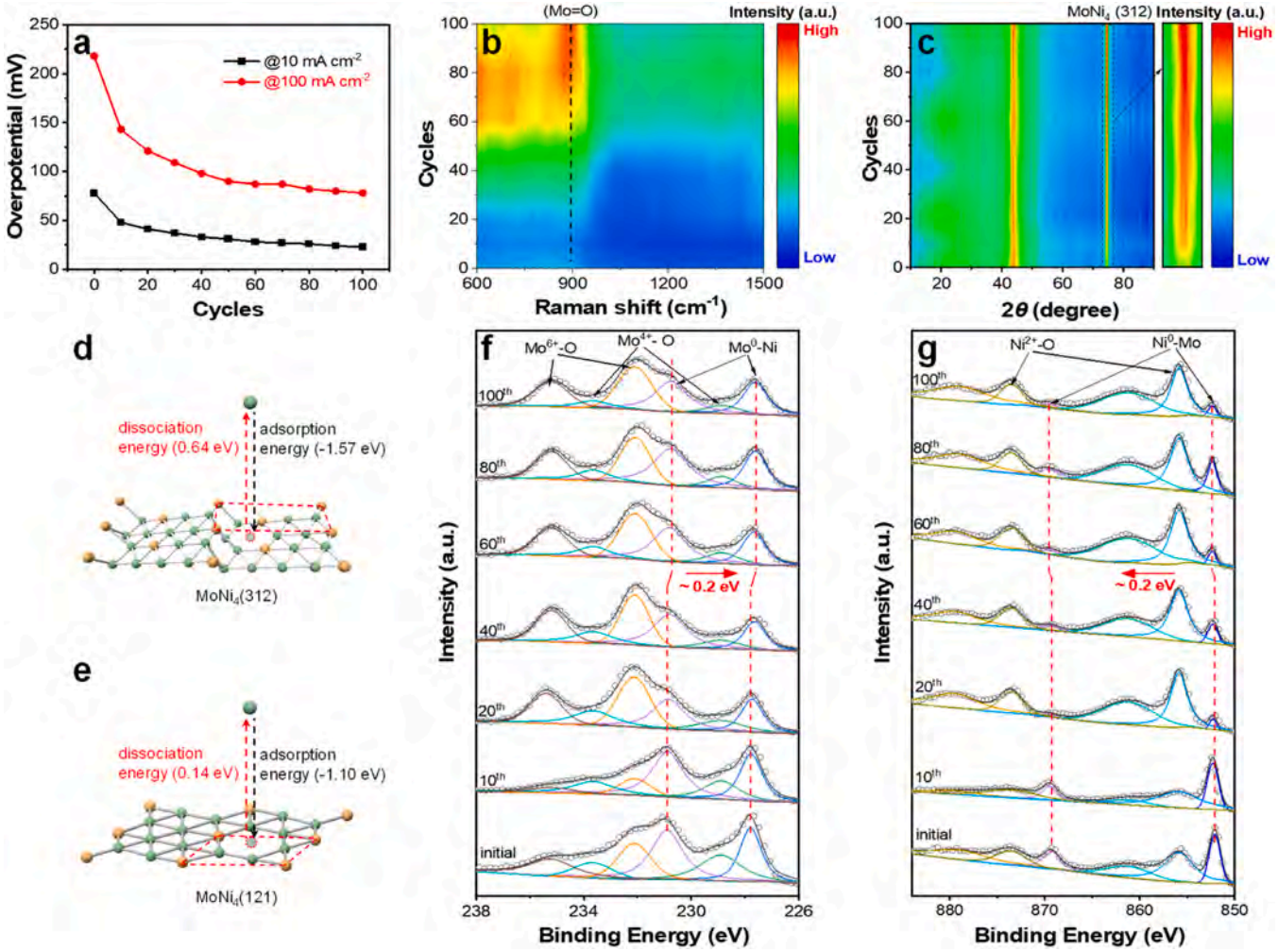

Fig. 2. (a) Overpotential variation of NM8 during the LSV scanning; *In situ* (b) Raman spectra and (c) XRD pattern during the LSV scanning; Adsorption and desorption energies of Ni ion on (d) $MoNi_4$(312) and (e) $MoNi_4$(121) crystal planes, respectively; High-resolution XPS of (f) Mo-3*d* and (g) Ni-2*p* of the NM8 catalyst during the LSV scanning.

electrocatalytic activity.

The morphology of NM8 after 100 LSV scans in Fig. S11 reveals no significant change compared to the pristine sample showing that the coating is composed of fine nanoparticles. The electrical conductivity also does not change after 100 LSV scans (Fig. S12) and the water contact angle on NM8 decreases from 87° to 76° after cycling, indicative of improved hydrophilicity (Fig. S13). This enhanced hydrophilicity is beneficial to mass transfer and reactant adsorption in aqueous electrolytes.

The *in situ* Raman scattering spectra in Figs. S14 and 2b reveal the changes in the surface species during the cycling process. The peak at 894 cm^{-1}, associated with the vibration of Mo═O, gradually intensifies due to the slight chemical dissolution of NM8 in 0.5 M H_2SO_4, resulting in the formation of molybdate and Ni^{2+} ions [28,29]. *In situ* XRD is performed to investigate the structural changes during LSV scanning (Figs. S15 and 2c). The intensity of the peak at $2\theta = 74.7°$ corresponding to the $MoNi_4$(312) plane increases, while the other peaks remain unchanged. The increase of the $MoNi_4$(312) signal confirms the oriented growth of this crystal plane. Consequently, the surface of NM8 has undergone reconstruction during the LSV scans, resulting in the enrichment of the $MoNi_4$(312) crystal plane. During the LSV scans, the negative potential at the NM8 cathode causes Ni^{2+} to adsorb onto it and generate a positive electric layer, followed by adsorption of MoO_4^{2-} ions onto the cathode. Subsequently, Ni and Mo on the surface are electrochemically reduced to directionally form the $MoNi_4$(312) crystal plane.

The orientated growth mechanism of the $MoNi_4$(312) crystal plane was explored by DFT calculation. The $MoNi_4$(312) and $MoNi_4$(121) surfaces, which are observed by XRD (Figs. 1b and 2c), are constructed to determine the adsorption and desorption energies of Ni species, respectively. The results indicate that Ni^{2+} adsorption onto the $MoNi_4$(312) crystal plane (–1.57 eV) is stronger than that on the $MoNi_4$(121) crystal plane (–1.10 eV), as shown in Fig. 2d. Consequently, Ni^{2+} ions are preferentially deposited on the $MoNi_4$(312) crystal plane to promote the growth of the $MoNi_4$(312) plane during the reconstruction process. Therefore, during the cycling process, the peak at 74.7° corresponding to the $MoNi_4$(312) crystal plane increases, while the peak at 43.5° corresponding to the $MoNi_4$(121) crystal plane remains unchanged. Moreover, the calculated desorption energies of Ni species on $MoNi_4$(312) and $MoNi_4$(121) impart more information about the superior corrosion resistance of the $MoNi_4$(312) plane, which has a larger desorption energy of 0.64 eV than 0.14 eV of the $MoNi_4$(121) plane (Fig. 2e), suggesting that the $MoNi_4$(312) plane has good stability.

XPS was carried out to determine the changes in the chemical states of NM8 during reconstruction. The high-resolution XPS spectra of Mo-3*d* in Fig. 2f show peaks at 227.8 and 230.9 eV associated with Mo^0-Ni in $MoNi_4$, which shift to lower binding energies by approximately 0.2 eV during reconstruction. However, the peaks at 228.9 and 233.6 eV associated with Mo^{4+}-O and those at 230.9 and 235.2 eV corresponding to Mo^{6+}-O of the surface-oxidized species show no significant change [30]. Fig. 2g displays the high-resolution XPS spectra of Ni-2*p*. The peaks at 852.1 and 869.3 eV associated with Ni^0-Mo in $MoNi_4$ shift to higher binding energies by approximately 0.2 eV, but those at 855.8 and 873.6 eV corresponding to Ni^{2+}-O in surface-oxidized species and the satellite peaks of Ni (861.2 and 879.5 eV) do not shift [31]. These results indicate that with the preferential growth of the $MoNi_4$(312) plane, strong interactions between Ni and Mo atoms on the $MoNi_4$(312) plane occur to facilitate electron transfer from Ni to Mo, possibly enhancing the HER catalytic performance.

3.3. HER performance

After 100 cycles of LSV scanning in 0.5 M H_2SO_4 for reconstruction, the samples are labelled as Ni-R, NM4-R, NM6-R, NM8-R, and NM10-R. The LSV curves and Tafel plots of these samples are displayed in Fig. S16. NM8-R and NM10-R have similar overpotentials and Tafel slopes, which are much smaller than those of Ni-R, NM4-R, and NM6-R. The HER performance of NM8-R, which has a rich exposure of the $MoNi_4$(312) plane, is studied in detail. The LSV curves in Fig. 3a show that the overpotential required for NM8-R to reach a current density of 10 mA cm^{-2} is 23 mV, which is much lower than that of SS and even comparable to that of the commercial Pt/C catalyst of 24 mV in 0.5 M H_2SO_4. The overpotential required by NM8-R to afford a current density of 200 mA cm^{-2} is 109 mV, which greatly exceeds the activity of the commercial Pt/C catalyst. In addition, NM8-R can produce a current density of 350 mA cm^{-2} at an overpotential of a mere 171 mV, indicating that NM8-R is commercially viable for large-current hydrogen production.

The Tafel slopes are obtained by fitting the linear regions of the Tafel plots. The Tafel slope of NM8-R (53.9 mV dec^{-1}) is close to that of commercial Pt/C (41.9 mV dec^{-1}) and smaller than that of SS (259.6 mV dec^{-1}) (Fig. 3b). The R_{ct} of NM8-R is comparable to that of commercial Pt/C and significantly smaller than that of SS (Figs. 3c and S17), confirming the fast HER kinetics of NM8-R. The HER characteristics of NM8-R is superior to those of previously reported Ni-based, Mo-based, and Ni-Mo-based electrocatalysts, including (1) Ni-BTC [32], (2) Mo-MoS_2 MSH/PC [33], (3) $MoS_{0.46}Te_{0.58}$/Gr [34], (4) Ni_2P-$Ni_{12}P_5$@Ni_3S_2/NF [35], (5) CPF-Fe/Ni [36], (6) $Re_{0.5}Mo_{0.5}S_2$ [37], (7) $Mo_2C(MoO_3)$ [38], (8) 6 % P-BMS [39], (9) PdNi NWs [40], (10) RuNi-Alloy@SC [41], (11) *W*-NiCo [42], (12) CoMoP-rGO/CNT [43], (13) MoS_2/Co-SAs-NS-CNTs@CoS_2/CC [44], (14) MoO_2-Mo_2C-NC@CC-950 ℃ [45], and (15) MoS_2 ML [46] as illustrated in Fig. 3d and Table S1. The comparison highlights the significant advantages of NM8-R with enriched $MoNi_4$(312) plane exposure. Additionally, the HER catalytic performance of NM8-R in an alkaline electrolyte (1.0 M KOH) was also investigated. It requires only 43 mV to achieve a current density of 10 mA cm^{-2}, with a Tafel slope of 92.4 mV dec^{-1} (Fig. S18). Although this performance is inferior to that in acidic media, it presents excellent alkaline HER.

The stability of NM8-R was assessed by multiple current steps and chronopotentiometry in 0.5 M H_2SO_4. The former indicates that the overpotentials are stable at current densities between 10 mA cm^{-2} and 200 mA cm^{-2} (Fig. S19), implying excellent robustness even at large current densities. Fig. 3e shows the durability of NM8-R at a current density of 100 mA cm^{-2} for 100 h, and the LSV curves before and after the durability test are nearly the same (Fig. S20). The FE-SEM images of NM8-R after the durability test in Fig. S21 are consistent with the ones before the test. Fig. S22 displays the XRD patterns of NM8-R before and after the test and similar diffraction patterns are observed, confirming that the structure and morphology of NM8-R are unchanged and the excellent stability. The hydrogen production rate and Faradaic efficiency (*FE*) of NM8-R were determined by the water displacement method (Fig. S23), in which 60.5 mL of hydrogen are produced by HER within 80 min at a constant current of 100 mA. The release rate of high-purity H_2 from 0.5 M H_2SO_4 is 1.85 mmol h^{-1} and the *FE* is as high as 99.5 % (Fig. 3f).

To assess the potential industrial scalability, NM8 electrodes of different geometrical sizes (1 × 1 cm^2, 2 × 2 cm^2, and 3 × 3 cm^2) shown in Fig. 3g were prepared by a similar protocol. Before the electrochemical measurement, the LSV scans of 100 cycles were conducted on NM8 (2 × 2 cm^2) and NM8 (3 × 3 cm^2) electrodes for surface reconstruction (Fig. S24). After the reconstruction, NM8 (2 × 2 cm^2) and NM8 (3 × 3 cm^2) also exhibited enhanced catalytic activity. The overpotentials of NM8 (2 × 2 cm^2) and NM8 (3 × 3 cm^2) at 10 mA cm^{-2} and 100 mA cm^{-2} for various scan numbers, as shown in Fig. S25, indicate a similar improvement trend in HER activity, consisting with the NM8 (1 × 1 cm^2). To achieve current densities of 10 mA cm^{-2} and 100 mA cm^{-2}, the overpotentials for NM8-R (2 × 2 cm^2) are 22.3 and 83.3 mV while are 21.0 and 84.3 mV for NM8-R (3 × 3 cm^2), as shown in the Fig. 3h. These results indicate that scaling up the geometrical size of the NM8 electrode by 8 folders (from 1 cm^2 to 9 cm^2) does not weaken the catalytic performance. More importantly, the NM8-R (3 × 3 cm^2) electrode generates currents of 100, 500, and 1000 mA at overpotentials of 21.9,

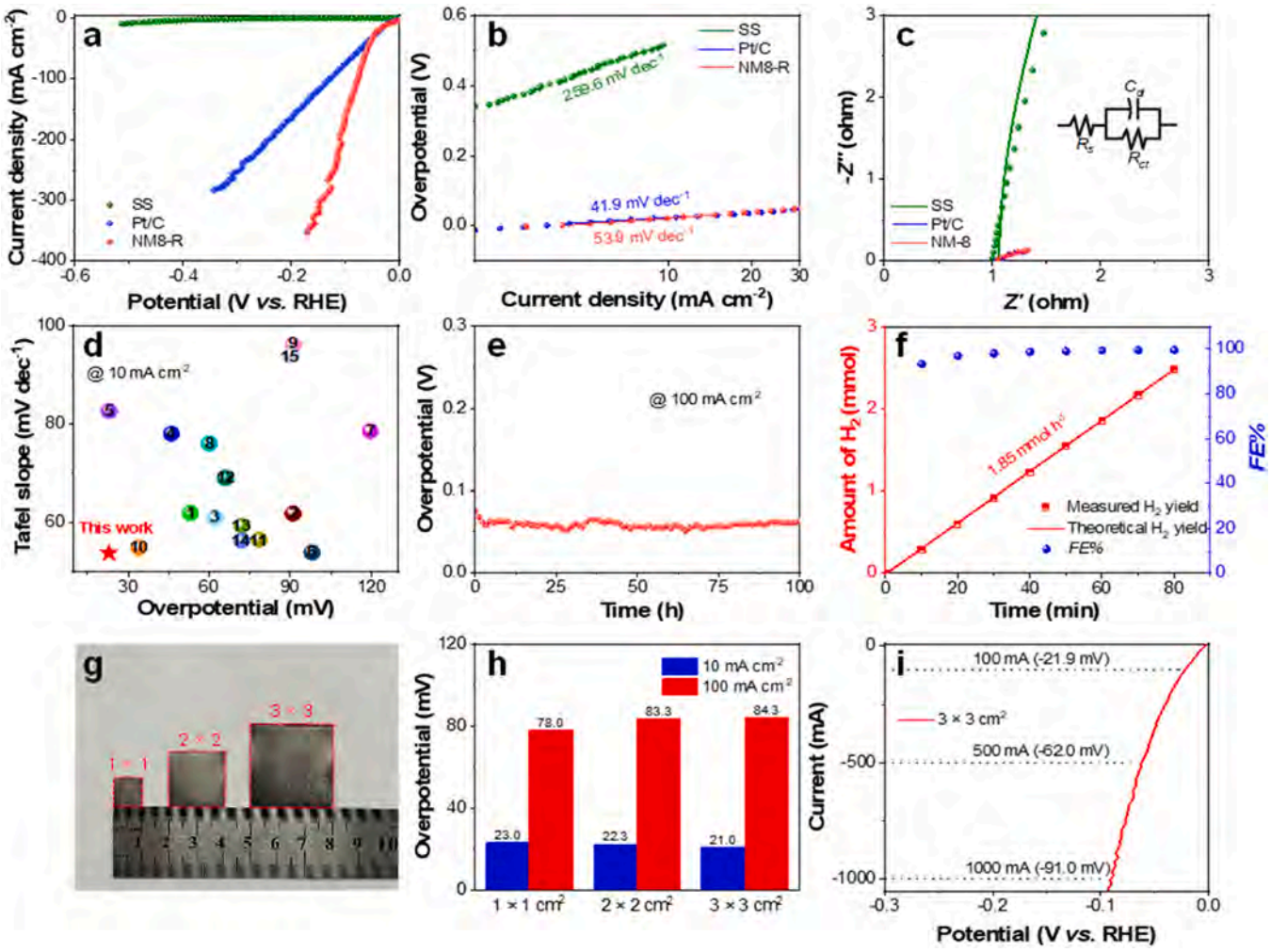

Fig. 3. HER properties: (a) LSV curves; (b) Tafel plots; (c) Nyquist plots; (d) Comparison of the overpotentials at 10 mA cm^{-2} and Tafel slopes of the electrocatalysts in the acidic electrolyte; (e) Stability; (f) Experimental and theoretical amounts of H_2 produced as well as *FE* at a current of 100 mA by NM8-R; (g) Photographs of the prepared NM8 of different geometrical sizes; (h) Comparison of overpotential for NM8-R of different geometrical sizes at current densities of 10 mA cm^{-2} and 100 mA cm^{-2}; (i) LSV curve of the NM8-R (3 × 3 cm^2) electrode.

62, and 91 mV (Fig. 3i), respectively, demonstrating excellent potential for industrial applications.

3.4. HER mechanism

The structural evolution process and the origin of the high activity of NM8-R were verified in detail using DFT calculations. $MoNi_4$(121) and $MoNi_4$(312) planes are used to construct the models according to XRD. Fig. 4a-b depicts the schematic diagrams of the simulated atomic structure of the $MoNi_4$(312) and $MoNi_4$(121) planes, respectively. The charge density distribution in Fig. 4c-d indicates that Mo atoms on the $MoNi_4$(312) surface are more negative than those on the $MoNi_4$(121) plane, whereas Ni exhibits the opposite trend. The average Mulliken charge of Mo atoms on the $MoNi_4$(312) plane is –0.267, which is lower than the value of –0.102 on the $MoNi_4$(121) plane (Fig. S26). On the other hand, Ni shows a value of 0.082 on the $MoNi_4$(312) plane, which is higher than 0.032 on the $MoNi_4$(121) plane. The results suggest more pronounced electron interactions among atoms on the $MoNi_4$(312) plane consistent with the results obtained by XPS.

The density of states (DOS) of $MoNi_4$(312) and $MoNi_4$(121) plane is shown in Fig. S27a-b. Compared to $MoNi_4$(121) plane, $MoNi_4$(312) has a more continuous DOS and a higher degree of orbital hybridization. The continuous DOS indicates that the electronic states of $MoNi_4$(312) plane are more dispersed and delocalized, enhancing electron conductivity and promoting electron transfer efficiency during electrochemical reactions [47]. Additionally, the higher degree of orbital hybridization in $MoNi_4$(312) plane provides more available electronic states, facilitating the activation of reactants and lowering the reaction energy barrier, thus accelerating the reaction rate [48]. The *d*-band center of the $MoNi_4$(312) plane downshifts in comparison with $MoNi_4$(121) (Fig. 4e), suggesting reduced adsorption of the reaction intermediates on this surface [49, 50]. This weakens the excessive adsorption capability of non-precious transition metals and enhances HER. [22] The H atom adsorption models of $MoNi_4$(312) and $MoNi_4$(121) plane for the calculation of the hydrogen adsorption energy are depicted in Figs. S28-S29. The Gibbs free energy (ΔG_{H^*}) of the Ni and Mo sites on $MoNi_4$(312) and $MoNi_4$(121) as shown in Fig. 4f. The ΔG_{H^*} at the Ni-(312) site is –0.71 eV, which is lower compared to the Ni-(121) site (–0.69 eV). In contrast, the ΔG_{H^*} at site Mo-(312) is –0.30 eV, which is higher than at the Mo-(121) site (–0.61 eV) and closer to zero. Therefore, on the $MoNi_4$(312) plane, Ni sites act as adsorption sites, while Mo sites serve as hydrogen desorption sites. During the HER process, hydrogen spontaneously adsorbs onto the Ni sites, then transfers to the Mo sites, and is ultimately released as hydrogen gas. The cooperative hydrogen production by Ni and Mo sites on the $MoNi_4$(312) plane results in a small barrier of rate-determining step (RDS) of 0.41 eV, which is lower than the 0.61 eV of the $MoNi_4$(121) plane. Our results reveal that the strong electronic interactions between atoms on the $MoNi_4$(312) plane result in

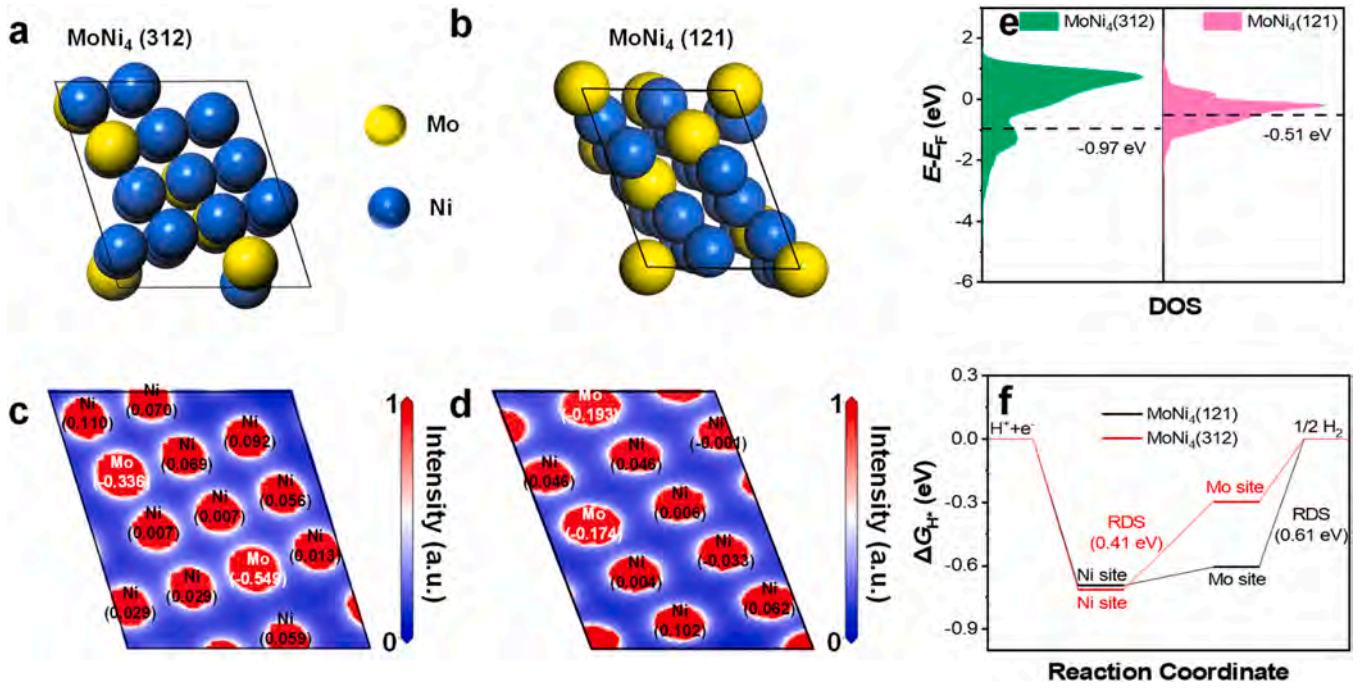

Fig. 4. Optimized structures of (a) $MoNi_4$(312) and (b) $MoNi_4$(121) surfaces; Charge density distributions (c) $MoNi_4$(312) and (d) $MoNi_4$(121) surfaces; (e) DOS of $MoNi_4$(312) and $MoNi_4$(121) with the *d*-band centers; (f) ΔG_{H^*} of the Ni and Mo sites on $MoNi_4$(312) and $MoNi_4$(121).

an optimized hydrogen adsorption process, giving rise to outstanding HER activity.

4. Conclusions

A Ni-Mo alloy catalyst, specifically $MoNi_4$ with the preferred crystal plane of (312), is designed and fabricated by electrodeposition and electrochemical reconstruction. The orientation-dependent growth of $MoNi_4$(312) enhances the electrocatalytic activity due to the strong Ni-Mo atomic interactions on the crystal plane and their synergistic catalysis of HER, which lower the reaction energy barrier. The catalyst (NM8-R) has remarkable electrochemical properties, including an overpotential of only 23.0 mV for a current density of 10 mA cm^{-2} in 0.5 M H_2SO_4. Moreover, the catalyst has excellent stability as inferred from continuous operation for 100 h at a current density of 100 mA cm^{-2} and a *FE* of 99.5 % for hydrogen production. This electrode can be scaled up controllably, and after reconstruction, NM8-R (3 × 3 cm^2) generates a current of 1 A at an overpotential of 91 mV. These results highlight the significant potential of the concept and catalyst for large-scale industrial hydrogen production. This study provides valuable insights into the orientational modulation of crystal facets for low-cost transition metal-based alloy electrocatalysts and enriches the understanding of crystal facet engineering.

CRediT authorship contribution statement

Song Xie: Methodology, Investigation, Roles/Writing – original draft, Visualization, and Writing – review & editing. **Chao Huang:** Methodology, Investigation, Roles/ Writing – original draft, Visualization, and Writing – review & editing. **Hao Dong:** Investigation, Data curation, Visualization, Formal analysis, and Writing – review & editing. **Baochai Xu:** Software, Visualization, and Writing – review & editing. **Yaping Miao:** Software, Visualization, and Writing – review & editing. **Biao Gao:** Methodology, Visualization, and Writing – review & editing. **Xuming Zhang:** Methodology, Funding acquisition, Validation, and Writing – review & editing. **Paul K. Chu:** Funding acquisition, Writing – review & editing, and Visualization. **Xiang Peng:** Conceptualization, Funding acquisition, Supervision, Writing – review & editing, Visualization, and Project administration.

Declaration of Competing Interest

The authors declare that they have no known competing financial interests or personal relationships that could have appeared to influence the work reported in this paper.

Acknowledgements

This work was financially supported by the National Natural Science Foundation of China (Nos. 52002294 and 22379116), Key Scientific Research Program of Department of Education of Hubei Province (No. D20231501), City University of Hong Kong Donation Research Grants (Nos. DON-RMG 9229021 and 9220061), and City University of Hong Kong Strategic Research Grant (SRG) (No. 7005505).

Appendix A. Supporting information

Supplementary data associated with this article can be found in the online version at doi:10.1016/j.apcatb.2024.124831.

Data availability

Data will be made available on request.

References

[1] X. Zhang, M. Schwarze, R. Schomäcker, R. Van de Krol, F.F. Abdi, Life cycle net energy assessment of sustainable H_2 production and hydrogenation of chemicals in a coupled photoelectrochemical device, Nat. Commun. 14 (2023) 991.
[2] F. Sun, J. Qin, Z. Wang, M. Yu, X. Wu, X. Sun, J. Qiu, Energy-saving hydrogen production by chlorine-free hybrid seawater splitting coupling hydrazine degradation, Nat. Commun. 12 (2021) 4182.
[3] L. Xiong, Y. Qiu, X. Peng, Z. Liu, P.K. Chu, Electronic structural engineering of transition metal-based electrocatalysts for the hydrogen evolution reaction, Nano Energy 104 (2022) 107882.
[4] S. Liu, Y. Shen, Y. Zhang, B. Cui, S. Xi, J. Zhang, L. Xu, S. Zhu, Y. Chen, Y. Deng, W. Hu, Extreme environmental thermal shock induced dislocation-rich Pt

nanoparticles boosting hydrogen evolution reaction, Adv. Mater. 34 (2022) 2106973.
[5] D. Guan, B. Wang, J. Zhang, R. Shi, K. Jiao, L. Li, Y. Wang, B. Xie, Q. Zhang, J. Yu, Y. Zhu, Z. Shao, M. Ni, Hydrogen society: from present to future, Energy Environ. Sci. 16 (2023) 4926–4943.
[6] X. Peng, Y. Yan, X. Jin, C. Huang, W. Jin, B. Gao, P.K. Chu, Recent advance and prospectives of electrocatalysts based on transition metal selenides for efficient water splitting, Nano Energy 78 (2020) 105234.
[7] S. Xie, H. Dong, X. Peng, Paul K. Chu, Non-precious electrocatalysts for the hydrogen evolution reaction, Innov. Discov. 1 (2024) 11.
[8] K.-H. Liu, H.-X. Zhong, S.-J. Li, Y.-X. Duan, M.-M. Shi, X.-B. Zhang, J.-M. Yan, Q. Jiang, Advanced catalysts for sustainable hydrogen generation and storage *Via* hydrogen evolution and carbon dioxide/nitrogen reduction reactions, Prog. Mater. Sci. 92 (2018) 64–111.
[9] S. Xie, H. Dong, E.I. Iwuoha, X. Peng, Phase transition of catalysts for advanced electrocatalysis, Coord. Chem. Rev. 514 (2024) 215920.
[10] H. Wu, C. Feng, L. Zhang, J. Zhang, D.P. Wilkinson, Non-noble metal electrocatalysts for the hydrogen evolution reaction in water electrolysis, Electrochem. Energy Rev. 4 (2021) 473–507.
[11] Y. Liu, J. Ding, F. Li, X. Su, Q. Zhang, G. Guan, F. Hu, J. Zhang, Q. Wang, Y. Jiang, B. Liu, H.B. Yang, Modulating hydrogen adsorption via charge transfer at the semiconductor–metal heterointerface for highly efficient hydrogen evolution catalysis, Adv. Mater. 35 (2023) 2207114.
[12] J.-T. Ren, L. Chen, H.-Y. Wang, Z.-Y. Yuan, High-entropy alloys in electrocatalysis: from fundamentals to applications, Chem. Soc. Rev. 52 (2023) 8319–8373.
[13] Z. Nie, L. Zhang, X. Ding, M. Cong, F. Xu, L. Ma, M. Guo, M. Li, L. Zhang, Catalytic kinetics regulation for enhanced electrochemical nitrogen oxidation by Ru-nanoclusters-coupled Mn_3O_4 catalysts decorated with atomically dispersed Ru atoms, Adv. Mater. 34 (2022) 2108180.
[14] Q. He, Y. Zhou, H. Shou, X. Wang, P. Zhang, W. Xu, S. Qiao, C. Wu, H. Liu, D. Liu, S. Chen, R. Long, Z. Qi, X. Wu, L. Song, Synergic reaction kinetics over adjacent ruthenium sites for superb hydrogen generation in alkaline media, Adv. Mater. 34 (2022) 2110604.
[15] Z. Zhu, M. Chen, M. Sun, J. Wang, Y. Zhou, X. Li, H. Tao, Mixture screening strategy of efficient transition metal heteronuclear dual-atom electrocatalysts toward nitrogen fixation, Phys. Chem. Chem. Phys. 24 (2022) 26776–26784.
[16] Y. Nakaya, S. Furukawa, Catalysis of alloys: classification, principles, and design for a variety of materials and reactions, Chem. Rev. 123 (2023) 5859–5947.
[17] C. Yang, R. Zhao, H. Xiang, J. Wu, W. Zhong, W. Li, Q. Zhang, N. Yang, X. Li, Ni-activated transition metal carbides for efficient hydrogen evolution in acidic and alkaline solutions, Adv. Energy Mater. 10 (2020) 2002260.
[18] M. Wang, H. Yang, J. Shi, Y. Chen, Y. Zhou, L. Wang, S. Di, X. Zhao, J. Zhong, T. Cheng, W. Zhou, Y. Li, Alloying nickel with molybdenum significantly accelerates alkaline hydrogen electrocatalysis, Angew. Chem. -Int. Ed. 60 (2021) 5771–5777.
[19] A. Nairan, P. Zou, C. Liang, J. Liu, D. Wu, P. Liu, C. Yang, NiMo solid solution nanowire array electrodes for highly efficient hydrogen evolution reaction, Adv. Funct. Mater. 29 (2019) 1903747.
[20] B.Y. Tang, R.P. Bisbey, K.M. Lodaya, W.L. Toh, Y. Surendranath, Reaction environment impacts charge transfer but not chemical reaction steps in hydrogen evolution catalysis, Nat. Catal. 6 (2023) 339–350.
[21] G. Kresse, J. Hafner, Ab initio molecular dynamics for liquid metals, Phys. Rev. B 47 (1993) 558–561.
[22] J.K. Nørskov, T. Bligaard, A. Logadottir, J. Kitchin, J.G. Chen, S. Pandelov, U. Stimming, Trends in the exchange current for hydrogen evolution, J. Electrochem. Soc. 152 (2005) J23.
[23] C. Pei, S. Chen, T. Zhao, M. Li, Z. Cui, B. Sun, S. Hu, S. Lan, H. Hahn, T. Feng, Nanostructured metallic glass in a highly upgraded energy state contributing to efficient catalytic performance, Adv. Mater. 34 (2022) 2200850.
[24] B. Zhong, S. Wan, P. Kuang, B. Cheng, L. Yu, J. Yu, Crystalline/amorphous Ni/Ni_xS_y supported on hierarchical porous nickel foam for high-current-density hydrogen evolution, Appl. Catal. B-Environ. 340 (2024) 123195.
[25] H. Su, X. Pan, S. Li, H. Zhang, R. Zou, Defect-engineered two-dimensional transition metal dichalcogenides towards electrocatalytic hydrogen evolution reaction, Carbon Energy 5 (2023) e296.
[26] B.-C. Xu, Y.-P. Miao, M.-Q. Mao, D.-L. Li, S. Xie, W.-H. Jin, S. Xiao, J. Wen, Z. Abd-Allah, Z.-T. Liu, X. Peng, P.K. Chu, Heterophase junction engineering-induced Co spin-state modulation of $CoSe_2$ for large-current hydrogen evolution reaction, Rare Met. 43 (2024) 2660–2670.
[27] X. Zheng, Y. Cao, X. Han, H. Liu, J. Wang, Z. Zhang, X. Wu, C. Zhong, W. Hu, Y. Deng, Pt embedded Ni_3Se_2@NiOOH core-shell dendrite-like nanoarrays on nickel as bifunctional electrocatalysts for overall water splitting, Sci. China Mater. 62 (2019) 1096–1104.
[28] W. Du, Y. Shi, W. Zhou, Y. Yu, B. Zhang, Unveiling the in situ dissolution and polymerization of Mo in Ni_4Mo alloy for promoting the hydrogen evolution reaction, Angew. Chem. Int. Ed. 60 (2021) 7051–7055.
[29] L.F. Huang, M.J. Hutchison, R.J. Santucci Jr., J.R. Scully, J.M. Rondinelli, Improved electrochemical phase diagrams from theory and experiment: The Ni-water system and its complex compounds, J. Phys. Chem. C. 121 (2017) 9782–9789.
[30] L. Chen, J. Shou, Y. Chen, W. Han, X. Tu, L. Zhang, Q. Sun, J. Cao, Y. Chang, H. Zheng, Efficient sunlight promoted nitrogen fixation from air under room temperature and ambient pressure via Ti/Mo composites, Chem. Eng. J. 451 (2023) 138592.
[31] B. Fei, Z. Chen, J. Liu, H. Xu, X. Yan, H. Qing, M. Chen, R. Wu, Ultrathinning nickel sulfide with modulated electron density for efficient water splitting, Adv. Energy Mater. 10 (2020) 2001963.
[32] M. Zhang, D. Hu, Z. Xu, B. Liu, M. Boubeche, Z. Chen, Y. Wang, H. Luo, K. Yan, Facile synthesis of Ni-, Co-, Cu-metal organic frameworks electrocatalyst boosting for hydrogen evolution reaction, J. Mater. Sci. Technol. 72 (2021) 172–179.
[33] Z. Sun, L. Lin, M. Yuan, H. Yao, Y. Deng, B. Huang, H. Li, G. Sun, J. Zhu, Mott-Schottky heterostructure induce the interfacial electron redistribution of MoS_2 for boosting pH-universal hydrogen evolution with Pt-like activity, Nano Energy 101 (2022) 107563.
[34] S. Sarwar, A. Ali, Y. Wang, M.R. Ahasan, R. Wang, A.J. Adamczyk, X. Zhang, Enhancement of hydrogen evolution reaction activity using metal-rich molybdenum sulfotelluride with graphene support: A combined experimental and computational study, Nano Energy 90 (2021) 106599.
[35] H. Yang, P. Guo, R. Wang, Z. Chen, H. Xu, H. Pan, D. Sun, F. Fang, R. Wu, Sequential phase conversion-induced phosphides heteronanorod arrays for superior hydrogen evolution performance to Pt in wide pH media, Adv. Mater. 34 (2022) 2107548.
[36] Y. Zang, D.-Q. Lu, K. Wang, B. Li, P. Peng, Y.-Q. Lan, S.-Q. Zang, A pyrolysis-free Ni/Fe bimetallic electrocatalyst for overall water splitting, Nat. Commun. 14 (2023) 1792.
[37] I.H. Kwak, T.T. Debela, I.S. Kwon, J. Seo, S.J. Yoo, J.-G. Kim, J.-P. Ahn, J. Park, H. S. Kang, Anisotropic alloying of $Re_{1-x}Mo_xS_2$ nanosheets to boost the electrochemical hydrogen evolution reaction, J. Mater. Chem. A 8 (2020) 25131–25141.
[38] A. Huang, H. Huang, F. Wang, N. Ke, C. Tan, L. Hao, X. Xu, Y. Xian, S. Agathopoulos, Mo_2C-based ceramic electrode with high stability and catalytic activity for hydrogen evolution reaction at high current density, Small 20 (2024) 2308068.
[39] Y. Qian, J. Yu, Z. Lyu, Q. Zhang, T.H. Lee, H. Pang, D.J. Kang, Durable hierarchical phosphorus-doped biphase MoS_2 electrocatalysts with enhanced H* adsorption, Carbon Energy 6 (2024) e376.
[40] L. Du, D. Feng, X. Xing, C. Wang, G.S. Armatas, D. Yang, Uniform palladium-nickel nanowires arrays for stable hydrogen leakage detection and efficient hydrogen evolution reaction, Chem. Eng. J. 400 (2020) 125864.
[41] X. Bai, Q.-Q. Pang, X. Du, S.-S. Yi, S. Zhang, J. Qian, X.-Z. Yue, Z.-Y. Liu, Integrating RuNi alloy in S-doped defective carbon for efficient hydrogen evolution in both acidic and alkaline media, Chem. Eng. J. 417 (2021) 129319.
[42] D. Gao, J. Guo, H. He, P. Xiao, Y. Zhang, Geometric and electronic modulation of fcc NiCo alloy by Group-VI B metal doping to accelerate hydrogen evolution reaction in acidic and alkaline media, Chem. Eng. J. 430 (2022) 133110.
[43] M. Chen, Z. Liu, X. Zhang, A. Zhong, W. Qin, W. Liu, Y. Liu, In-situ phosphatizing of cobalt-molybdenum nanosheet arrays on self-supporting rGO/CNTs film as efficient electrocatalysts for hydrogen evolution reaction, Chem. Eng. J. 422 (2021) 130355.
[44] B. Liu, Y. Cheng, B. Cao, M. Hu, P. Jing, R. Gao, Y. Du, J. Zhang, J. Liu, Hybrid heterojunction of molybdenum disulfide/single cobalt atoms anchored nitrogen, sulfur-doped carbon nanotube/cobalt disulfide with multiple active sites for highly efficient hydrogen evolution, Appl. Catal. B-Environ. 298 (2021) 120630.
[45] J. Huang, Y. Liu, L. Wang, Z. Hou, Z. Zhang, X. Zhang, J. Liu, Coupling interactions enhancing molybdenum-based electrocatalysts for high-efficiency hydrogen evolution at wide pH, Chem. Eng. J. 469 (2023) 143908.
[46] J. Qu, Y. Li, F. Li, T. Li, X. Wang, Y. Yin, L. Ma, O.G. Schmidt, F. Zhu, Direct thermal enhancement of hydrogen evolution reaction of on-chip monolayer MoS_2, ACS Nano 16 (2022) 2921–2927.
[47] X. Qin, B. Yan, T. Chen, Z. Teng, D.K. Cho, A. Haryanto, H.W. Lim, C.W. Lee, Y. Piao, L. Xu, J.Y. Kim, Customized electronic modulations of transition metal chalcogenide electrodes via heterointerfacing/high-valence doping toward high-performance water electrolysis with ampere-level current density, Adv. Funct. Mater. 34 (2024) 2405262.
[48] X. Zhou, J. Li, G. Zhou, W. Huang, Y. Zhang, J. Yang, H. Pang, M. Zhang, D. Sun, Y. Tang, L. Xu, Manipulating *d-d* orbital hybridization induced by Mo-doped Co_9S_8 nanorod arrays for high-efficiency water electrolysis, J. Energy Chem. 93 (2024) 592–600.
[49] Z. Hu, L. Zhang, J. Huang, Z. Feng, Q. Xiong, Z. Ye, Z. Chen, X. Li, Z. Yu, Self-supported nickel-doped molybdenum carbide nanoflower clusters on carbon fiber paper for an efficient hydrogen evolution reaction, Nanoscale 13 (2021) 8264–8274.
[50] L. Zhang, Z. Hu, J. Huang, Z. Chen, X. Li, Z. Feng, H. Yang, S. Huang, R. Luo, Experimental and DFT studies of flower-like Ni-doped Mo_2C on carbon fiber paper: A highly efficient and robust HER electrocatalyst modulated by $Ni(NO_3)_2$ concentration, J. Adv. Ceram. 11 (2022) 1294–1306.

Supporting Information

A $MoNi_4$(312) surface preferred reconstruction enhancing hydrogen evolution

Song Xie[1,5], Chao Huang[2,5], Hao Dong[1], Baochai Xu[1], Yaping Miao[3], Biao Gao[4], Xuming Zhang[4], Paul K. Chu[2], Xiang Peng[1]*

[1] Hubei Key Laboratory of Plasma Chemistry and Advanced Materials, Engineering Research Center of Phosphorus Resources Development and Utilization of Ministry of Education, School of Materials Science and Engineering, Wuhan Institute of Technology, Wuhan 430205, China

[2] Department of Physics, Department of Materials Science and Engineering, and Department of Biomedical Engineering, City University of Hong Kong, Tat Chee Avenue, Kowloon, Hong Kong, China

[3] School of Textile Science and Engineering, Xi'an Polytechnic University, Xi'an 710048, China

[4] The State Key Laboratory of Refractories and Metallurgy, Institute of Advanced Materials and Nanotechnology, Wuhan University of Science and Technology, Wuhan 430081, China

[5] These authors contributed equally to this work.

*Correspondence: xpeng@wit.edu.cn (X. P.)

Faradaic efficiency calculation

The Faradaic efficiency (*FE*) describes the efficiency of charge transfer in an electrochemical reaction and is expressed as:

$$FE = \frac{n(H_2)_M}{n(H_2)_T} \times 100\%, \qquad \text{(Eq. S1)}$$

where $n(H_2)_M$ (mol) is the molar mass of measured hydrogen and $n(H_2)_T$ (mol) is the theoretical molar mass of total hydrogen produced. Additionally,

$$n(H_2)_M = \frac{V_L}{V_m}, \qquad \text{(Eq. S2)}$$

where V_L (L) is the volume of hydrogen produced, V_m (L mol^{-1}) is the molar volume of the gas at room temperature, and V_m is 24.45 L mol^{-1} at 298.15 K and 1.013×10^5 Pa.

$$n(H_2)_T = \frac{i \times t}{2 \times F}, \qquad \text{(Eq. S3)}$$

where i (A) is the current, t (s) is the time duration, and F is Faraday's constant. *FE* is calculated to be 99.5% at an applied current of 100 mA for 80 min.

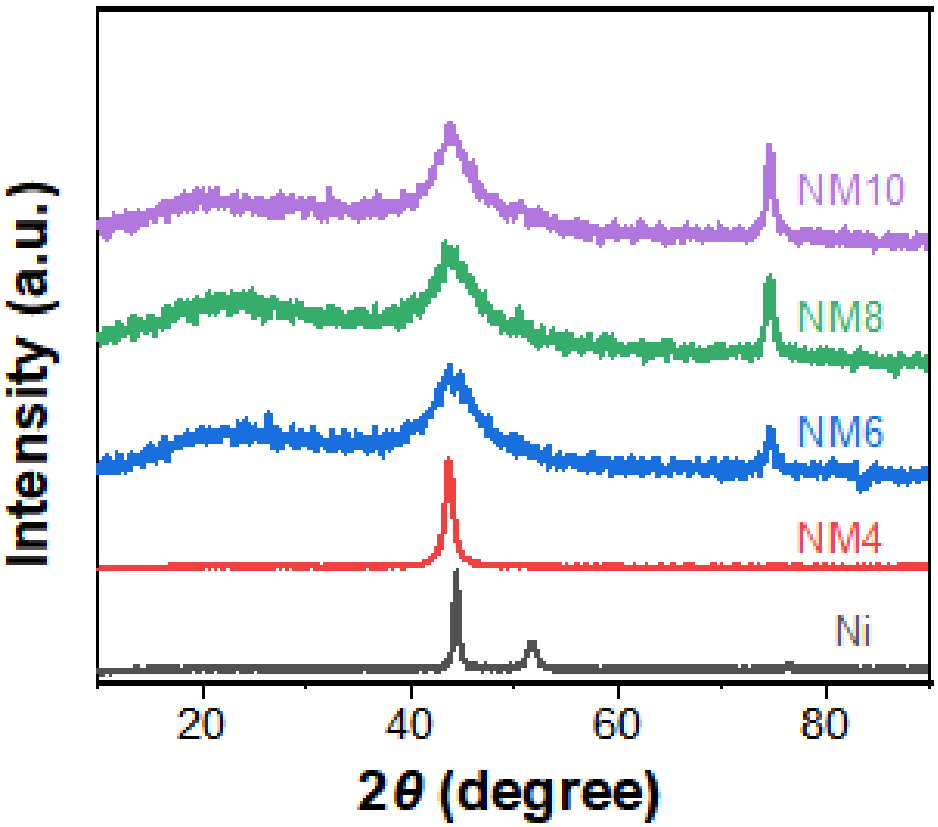

Figure S1. XRD patterns of Ni, NM4, NM6, NM8, and NM10.

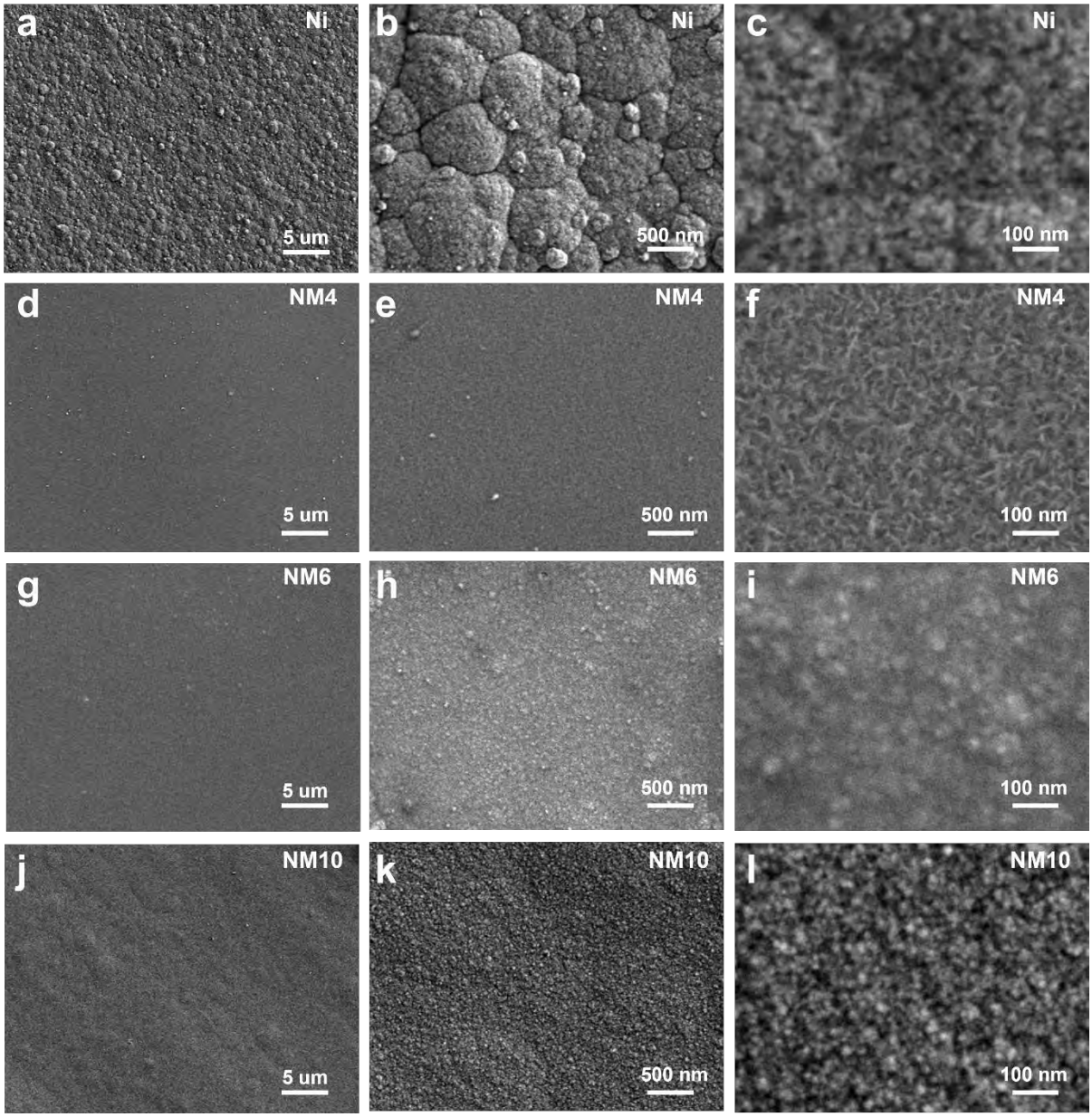

Figure S2. FE-SEM images: (a-c) Ni, (d-f) NM4, (g-i) NM6, and (j-l) NM10.

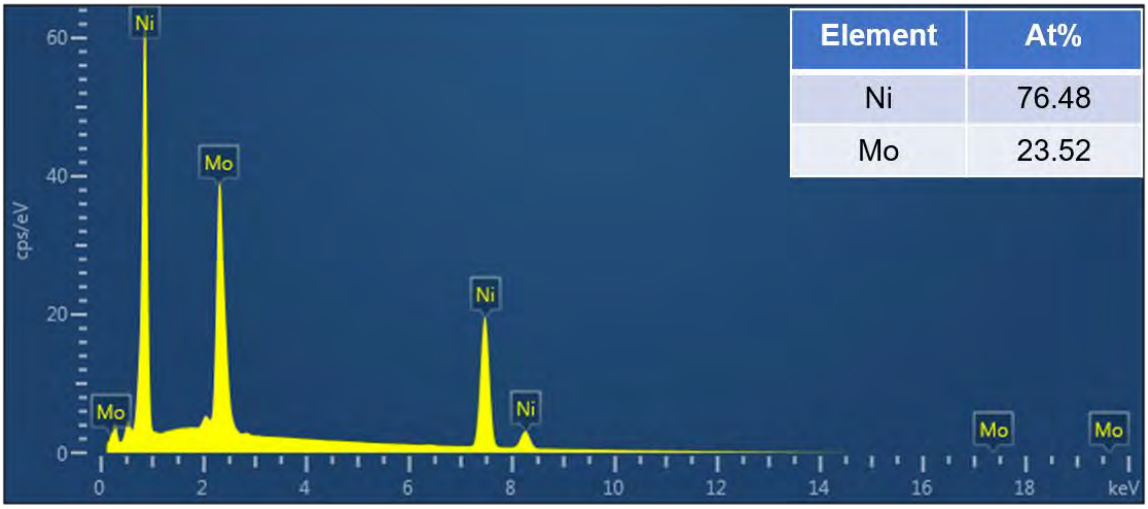

Figure S3. Elemental contents of Ni and Mo in NM8.

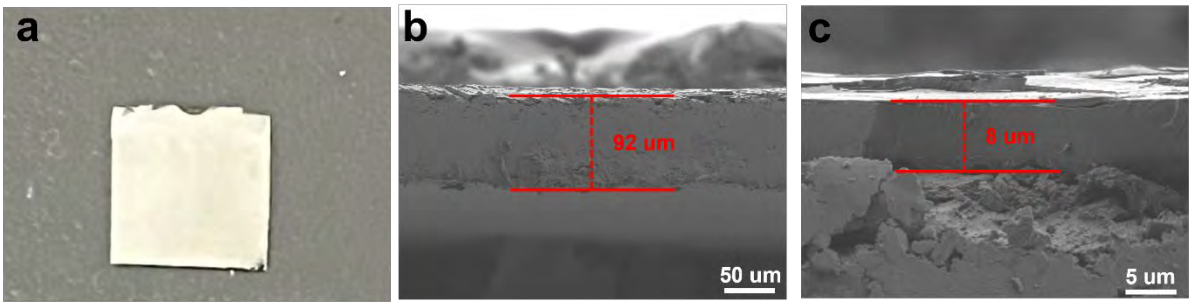

Figure S4. Photographs of (a) NM8; (b-c) Cross-sectional FE-SEM images of NM8.

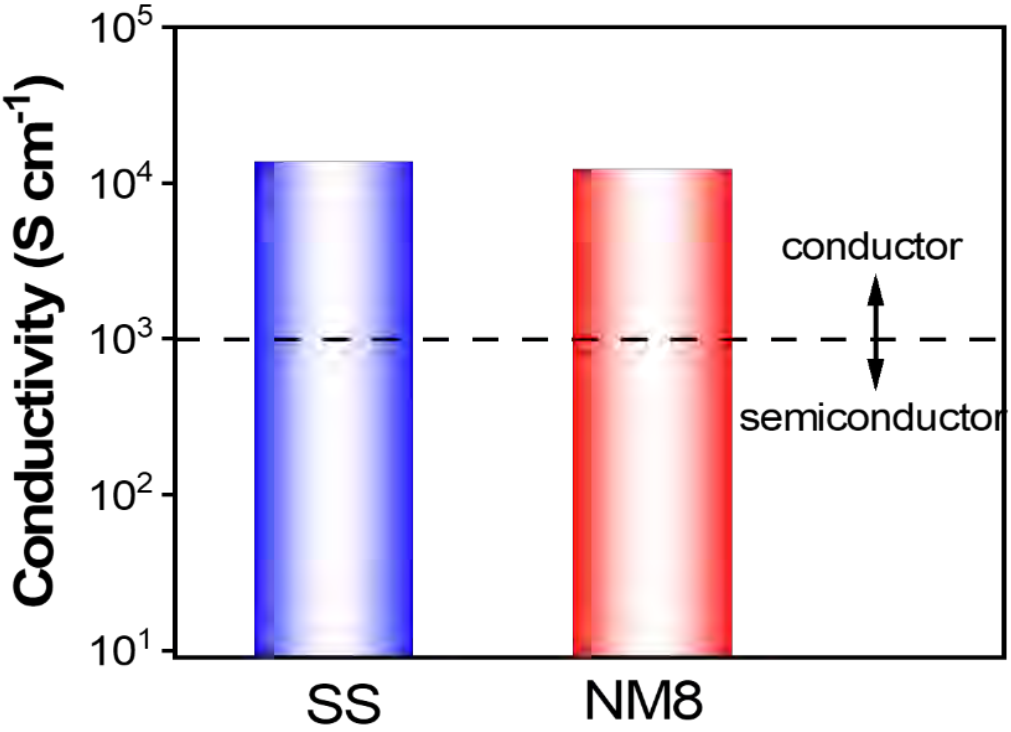

Figure S5. Electrical conductivity of SS and NM8.

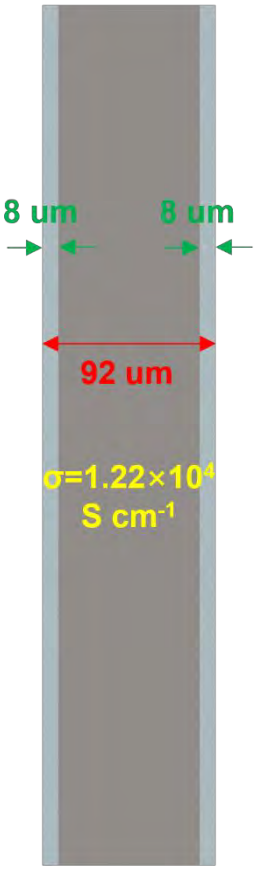

Figure S6. Schematic diagram of the structure of NM8.

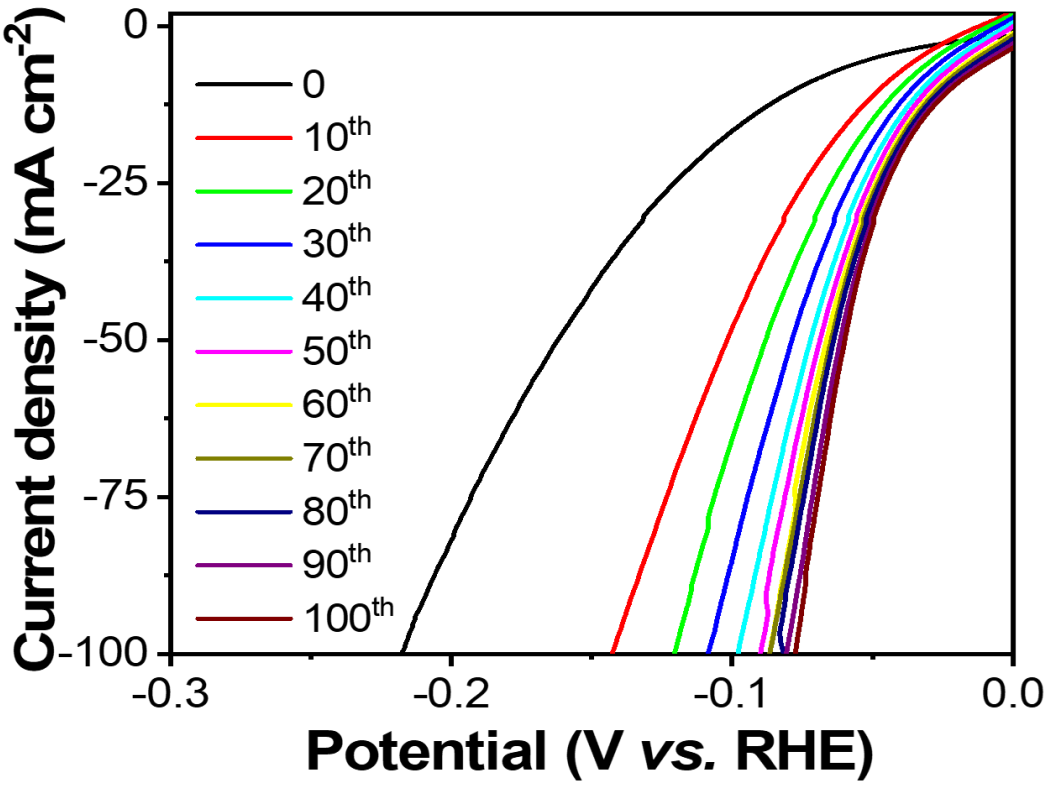

Figure S7. LSV curves of the initial 100 scans acquired from NM8 in 0.5 M H_2SO_4.

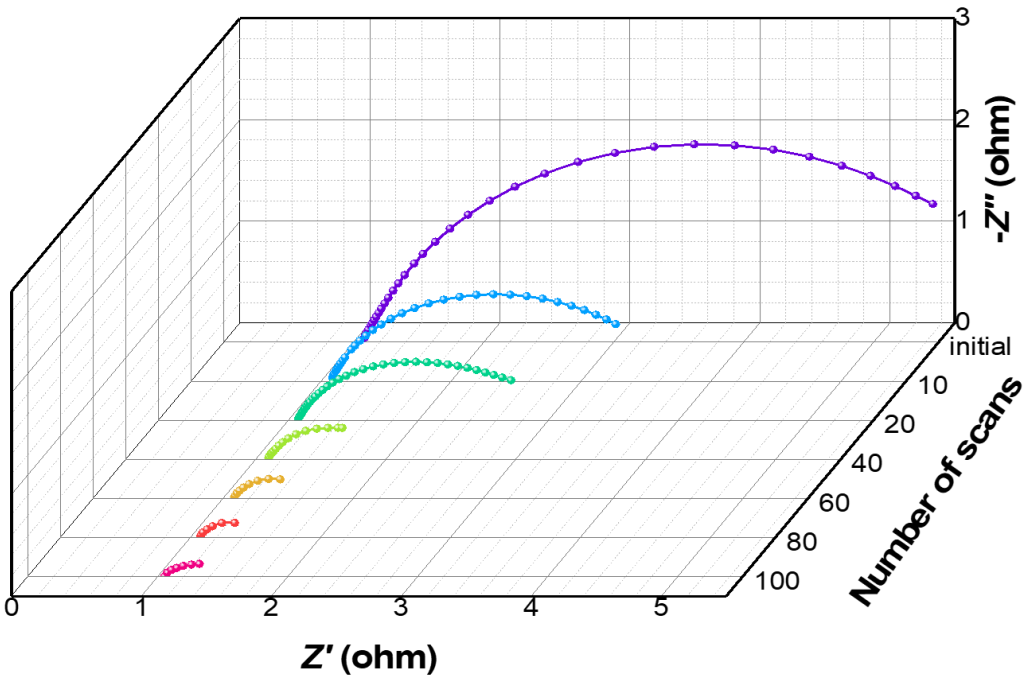

Figure S8. *In situ* Nyquist plots of NM8 during LSV scans.

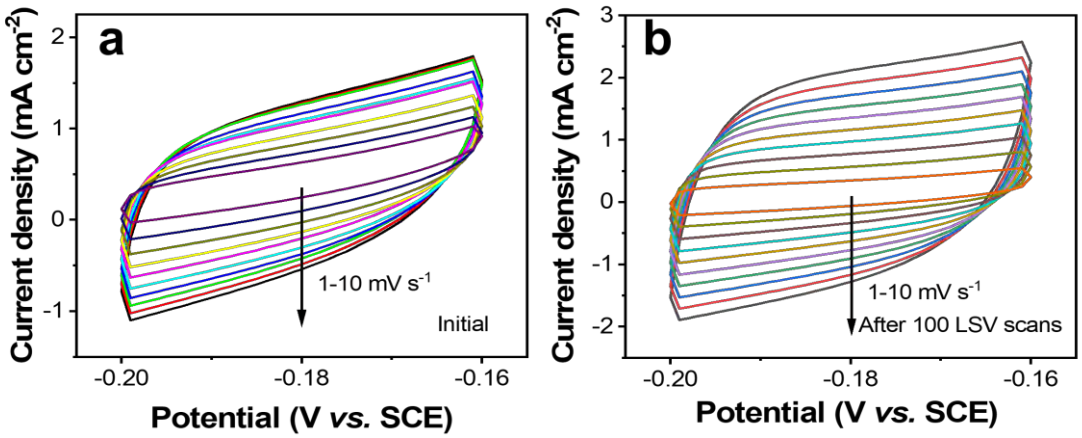

Figure S9. Cyclic voltammetry curves of NM8 before and after 100 LSV scans at scanning rates from 1 to 10 mV s^{-1}**.**

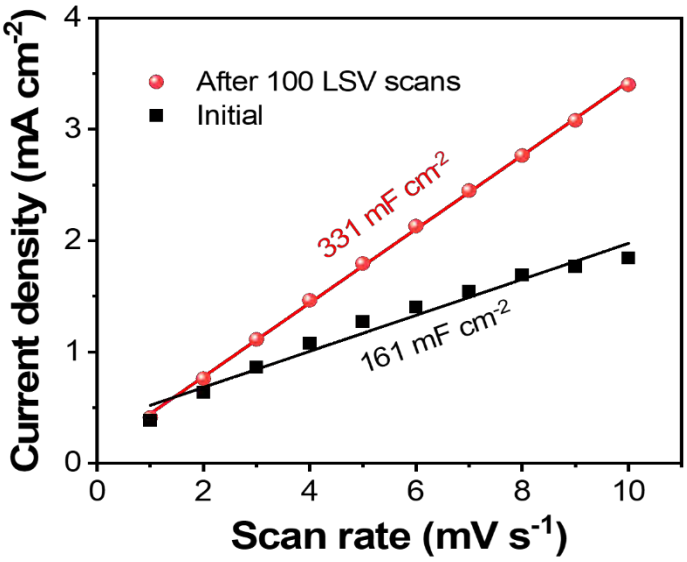

Figure S10. Electrochemically active surface area of NM8 before and after 100 LSV scans.

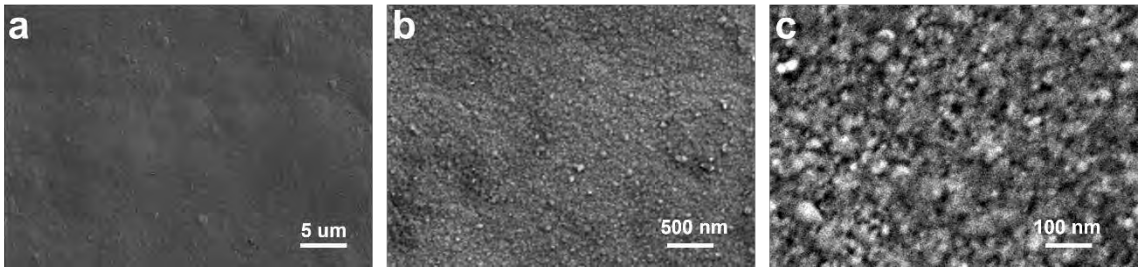

Figure S11. FE-SEM images of NM8 after 100 LSV scans.

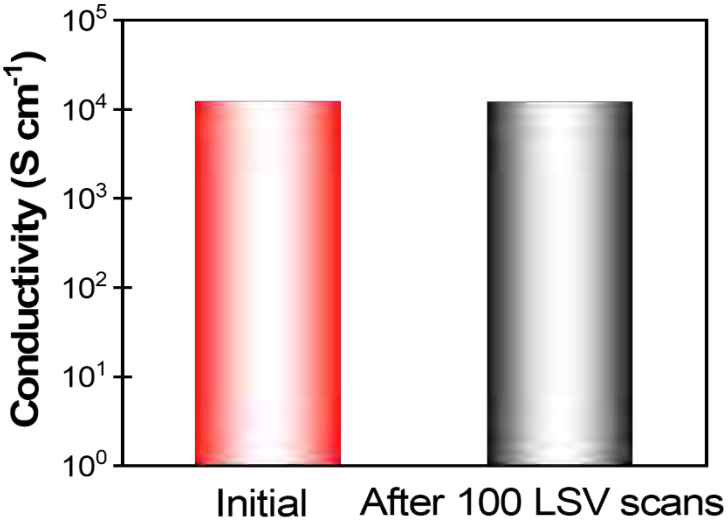

Figure S12. Electrical conductivity of NM8 before and after 100 LSV scans.

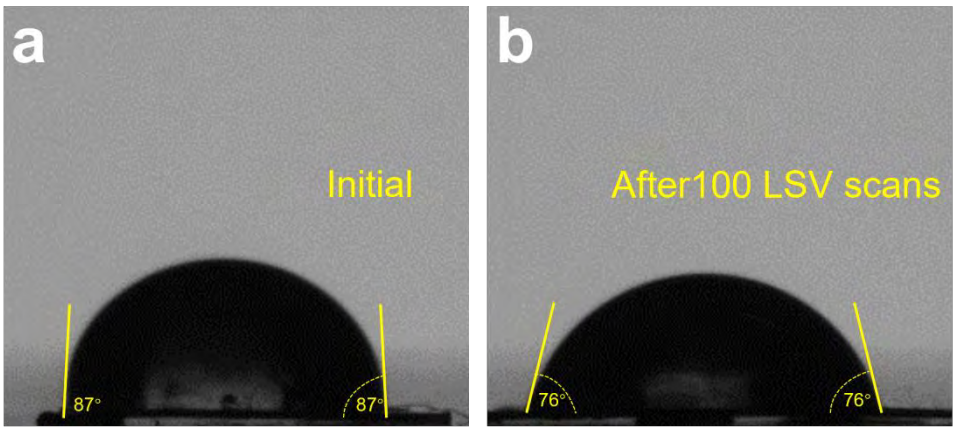

Figure S13. Water droplet contact angle images of NM8 before and after LSV scanning.

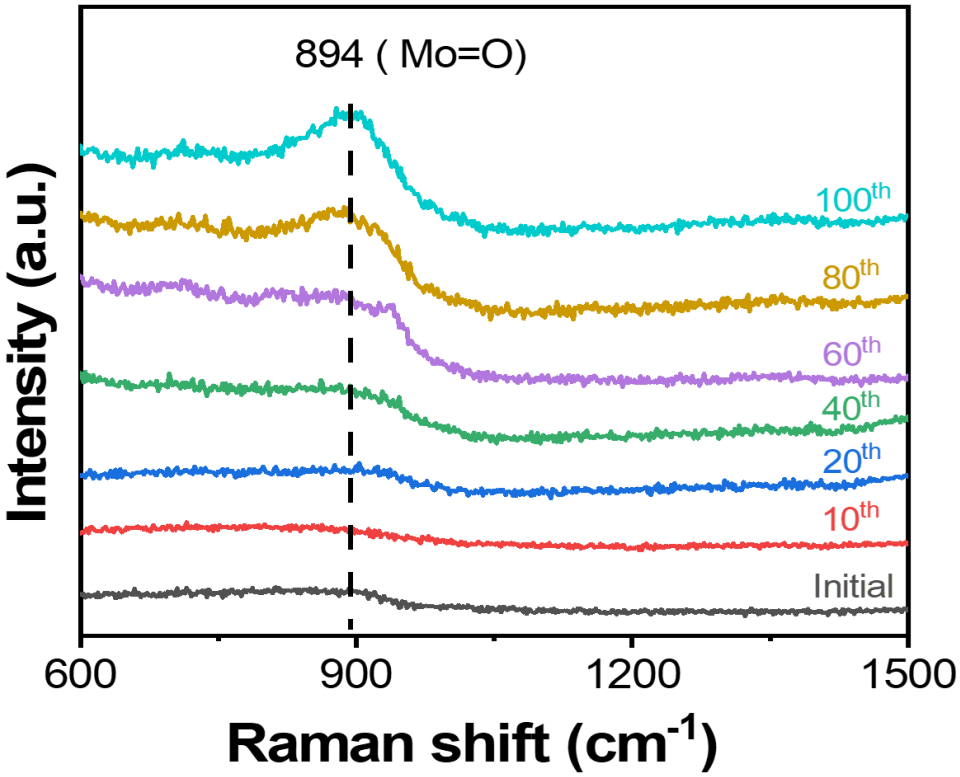

Figure S14. *In situ* Raman scattering spectra of NM8 during LSV scanning.

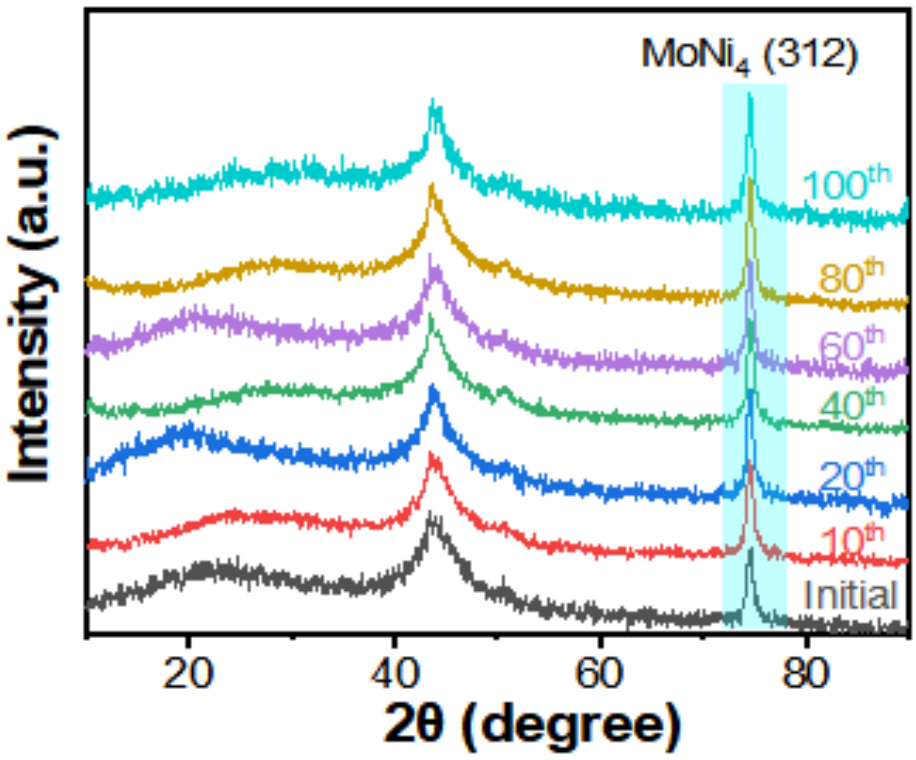

Figure S15. *In situ* XRD patterns of NM8 during LSV scanning.

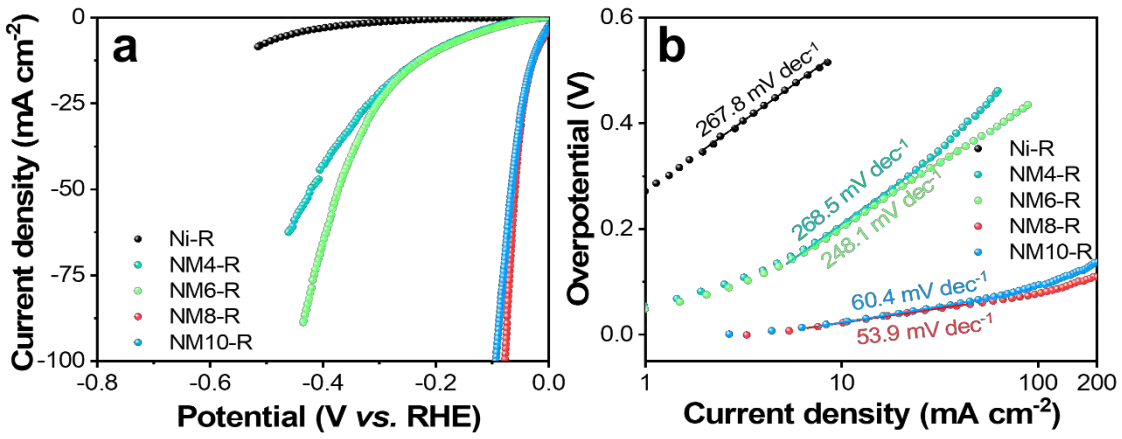

Figure S16. (a) LSV curves and (b) Tafel plots of Ni-R, NM4-R, NM6-R, NM8-R, and NM10-R in 0.5 M H_2SO_4.

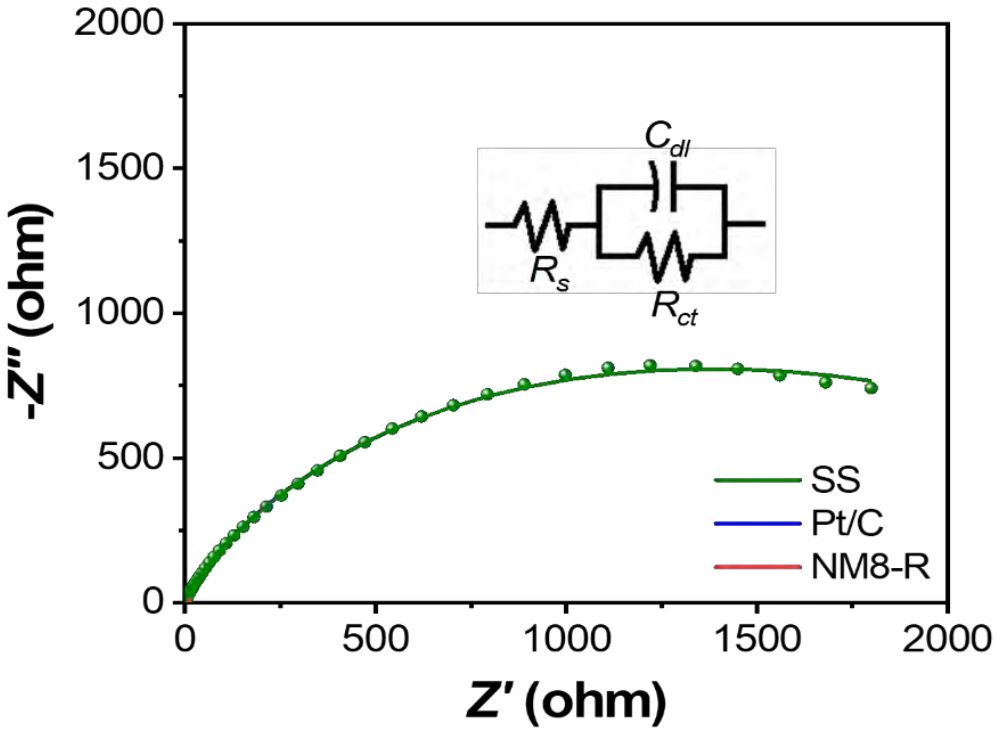

Figure S17. Nyquist curves of NM8-R, commercial Pt/C, and bare SS.

Table S1. Comparison of the overpotentials and Tafel slopes of different catalysts.

Number	Catalysts	Overpotential at 10 mA cm^{-2} (mV)	Tafel slope (mV dec^{-1})
1	Ni-BTC[1]	53	62
2	Mo-MoS_2 MSH/PC[2]	91	61.9
3	$MoS_{0.46}Te_{0.58}$/Gr[3]	62.2	61.1
4	Ni_2P-$Ni_{12}P_5$@Ni_3S_2/NF[4]	46	78
5	CPF-Fe/Ni[5]	23	82.6
6	$Re_{0.5}Mo_{0.5}S_2$[6]	98	54
7	Mo_2C(MoO_3)[7]	119.5	78.5
8	6% P-BMS[8]	60	76
9	PdNi NWs[9]	91	96
10	RuNi-Alloy@SC[10]	34	55
11	*W*-NiCo[11]	78.5	56.6
12	CoMoP-rGO/CNT[12]	66	69
13	MoS_2/CoSAs-NS-CNTs@CoS_2/CC[13]	72	59.4
14	MoO_2-Mo_2C-NC@CC-950 °C[14]	72	56.42
15	MoS_2 ML[15]	90	94
This work	NM8-R	23	53.9

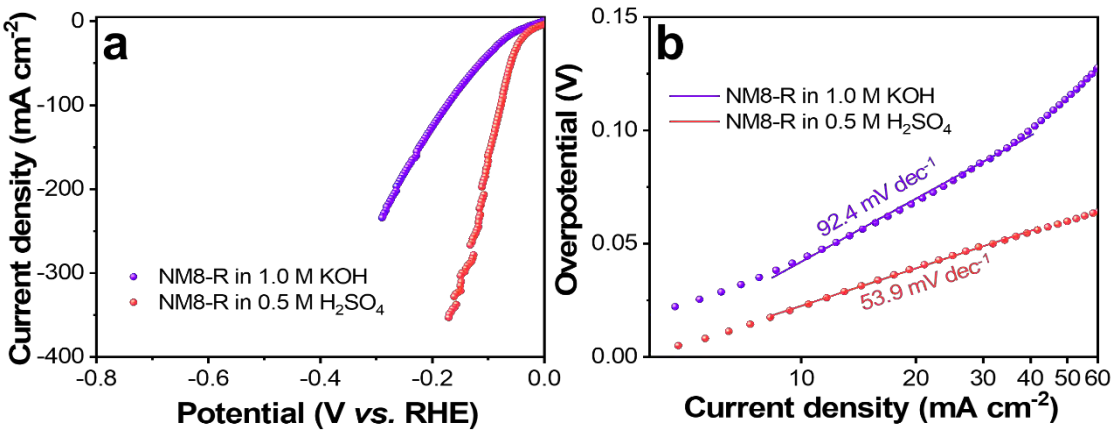

Figure S18. (a) LSV curves and (b)Tafel plots of NM8-R in acidic (0.5 M H_2SO_4) and alkaline (1.0 M KOH) electrolytes.

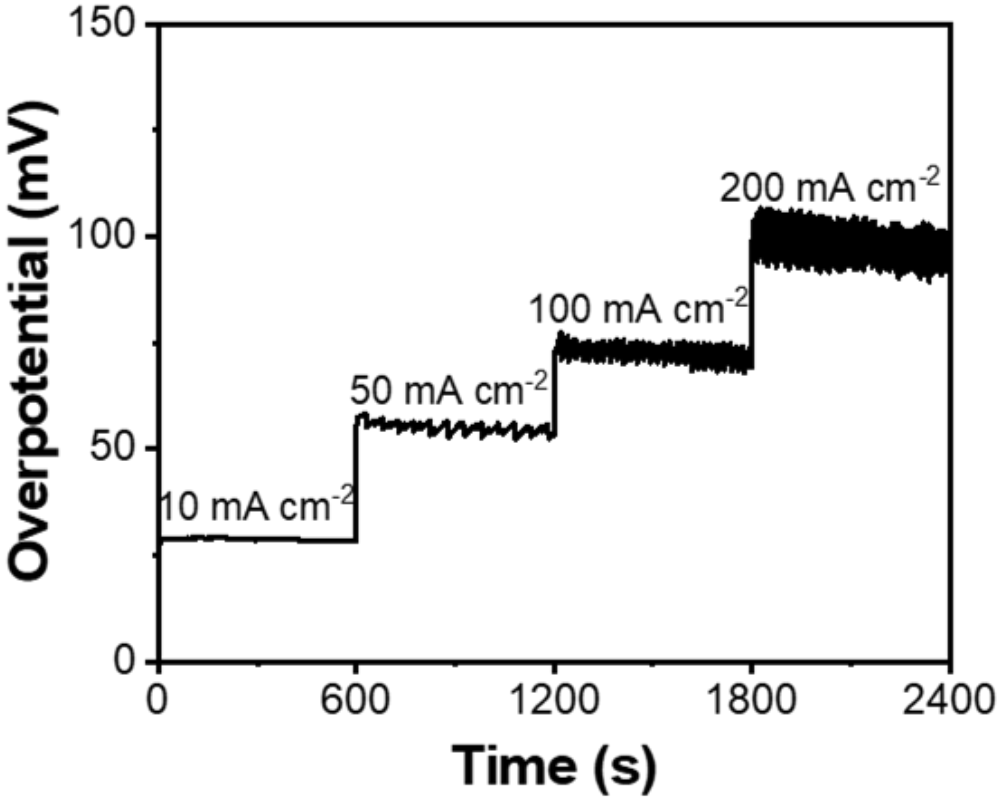

Figure S19. Multiple current step plot of NM8-R.

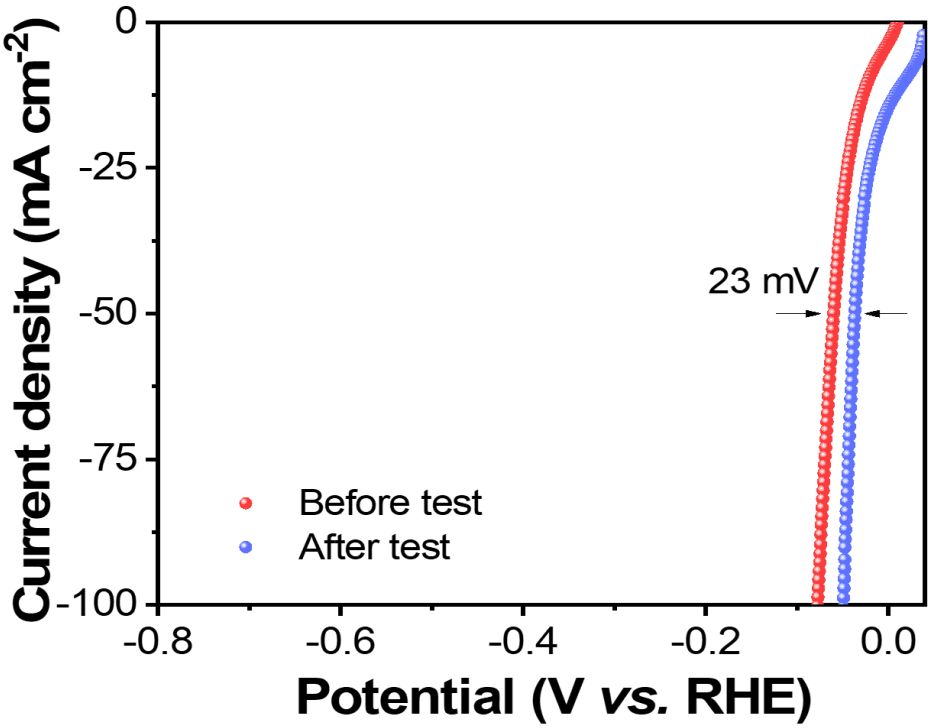

Figure S20. LSV curves of NM8-R before and after long-term measurements.

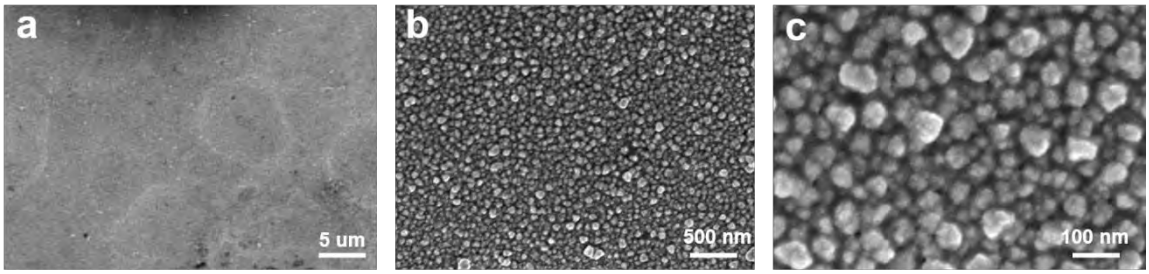

Figure S21. FE-SEM images of NM8-R after long-term measurements.

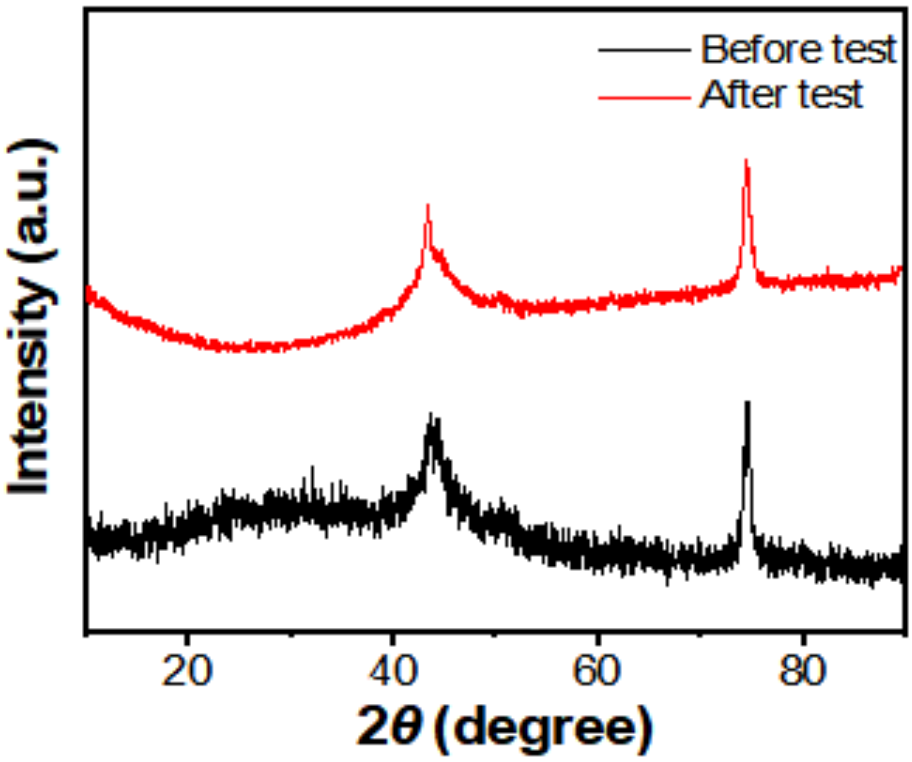

Figure S22. XRD patterns of NM8-R before and after long-term measurements.

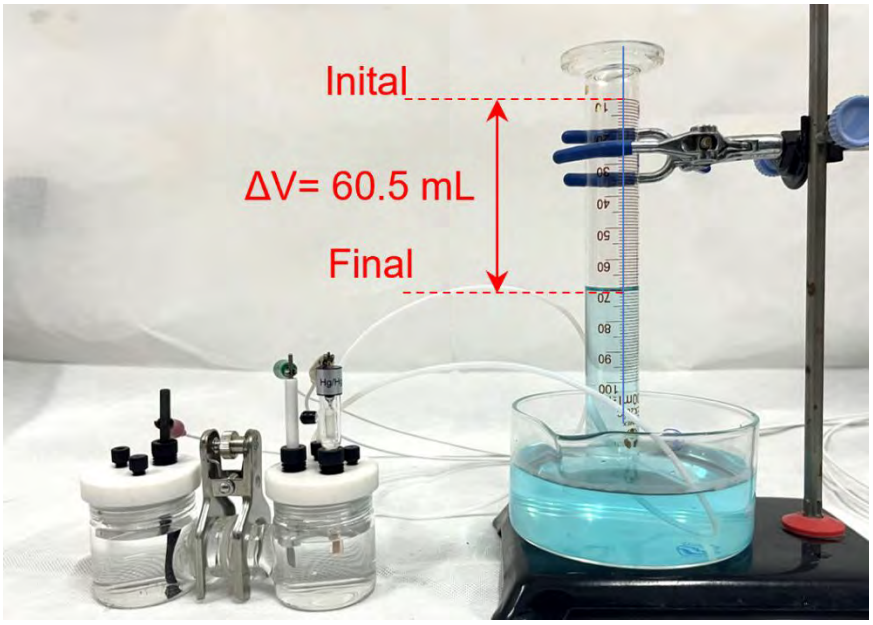

Figure S23. Photograph of the water splitting system with the NM8-R catalyst as the working electrode for the assessment of H_2 production by the water displacement method.

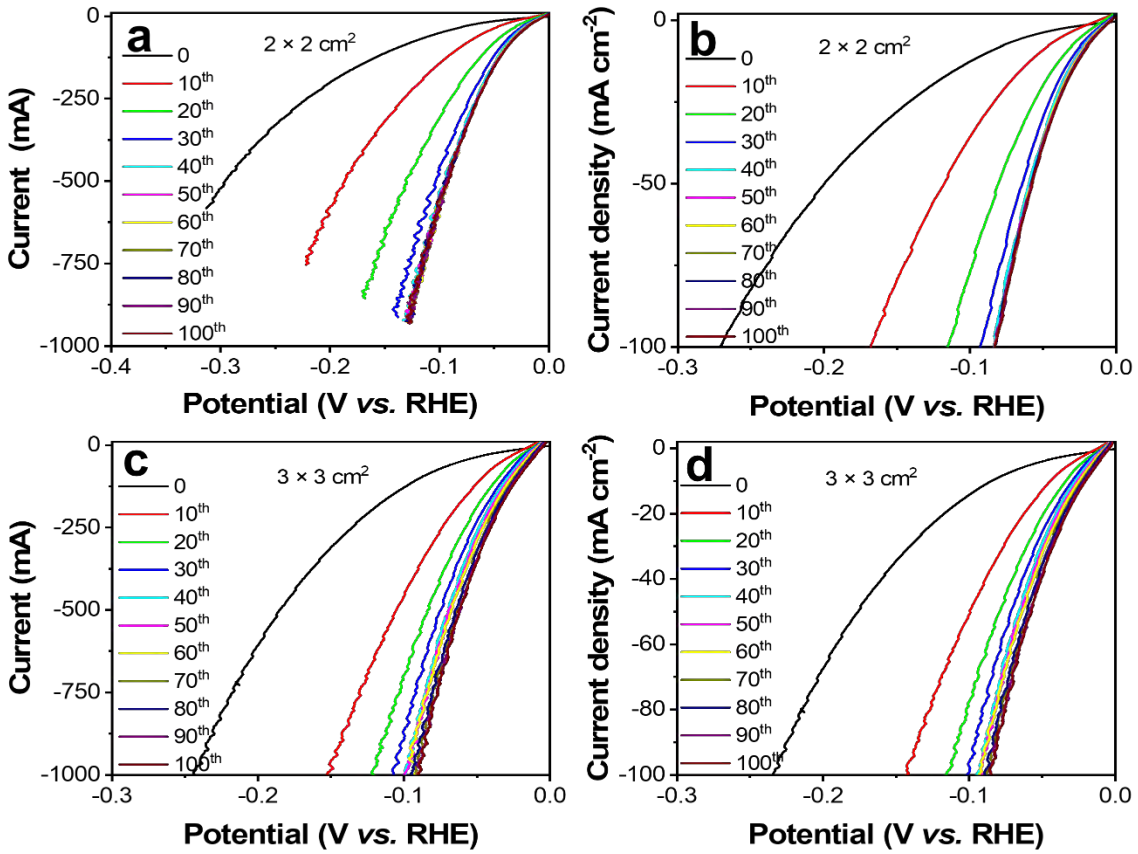

Figure S24. LSV curves of the initial 100 scans acquired from (a-b) 2 × 2 cm^2 NM8 and (c-d) 3 × 3 cm^2 NM8 in 0.5 M H_2SO_4.

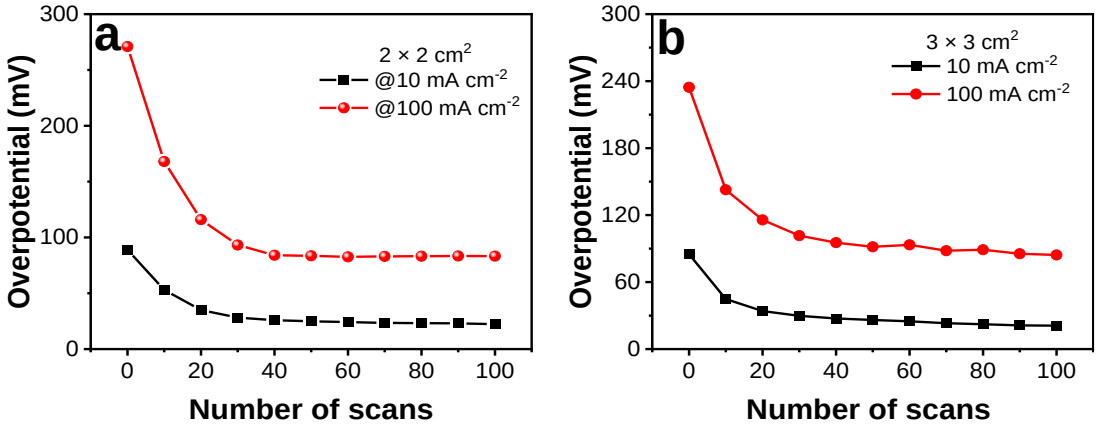

Figure S25. Overpotential variation of (a) 2 × 2 cm^2 NM8 and (b) 3 × 3 cm^2 NM8 during the LSV scanning in 0.5 M H_2SO_4.

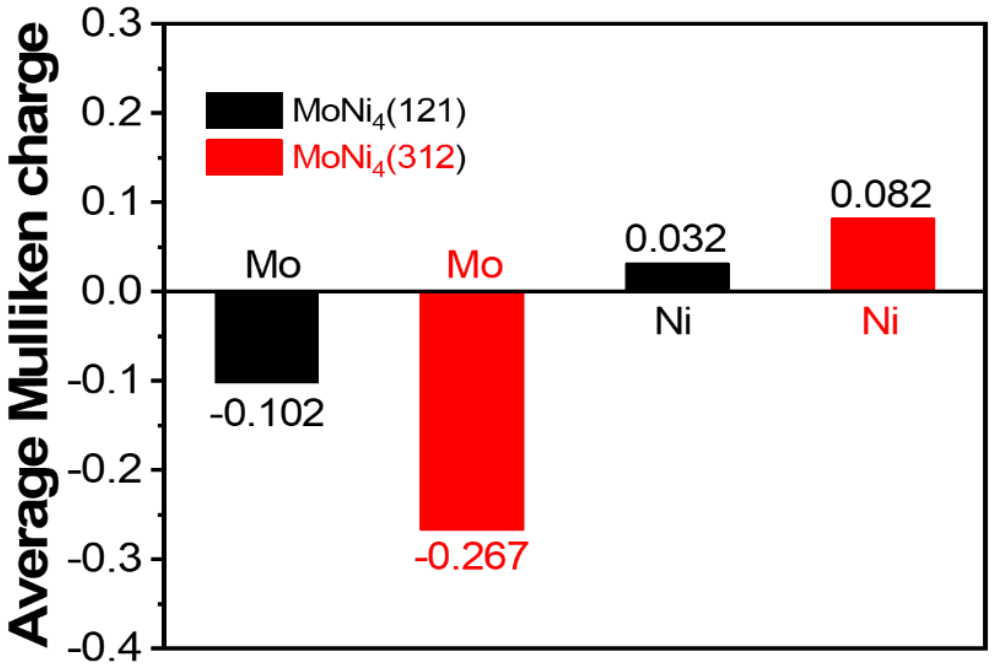

Figure S26. Average Mulliken electron distributions of Ni and Mo on the $MoNi_4$(312) and $MoNi_4$(121) crystal planes.

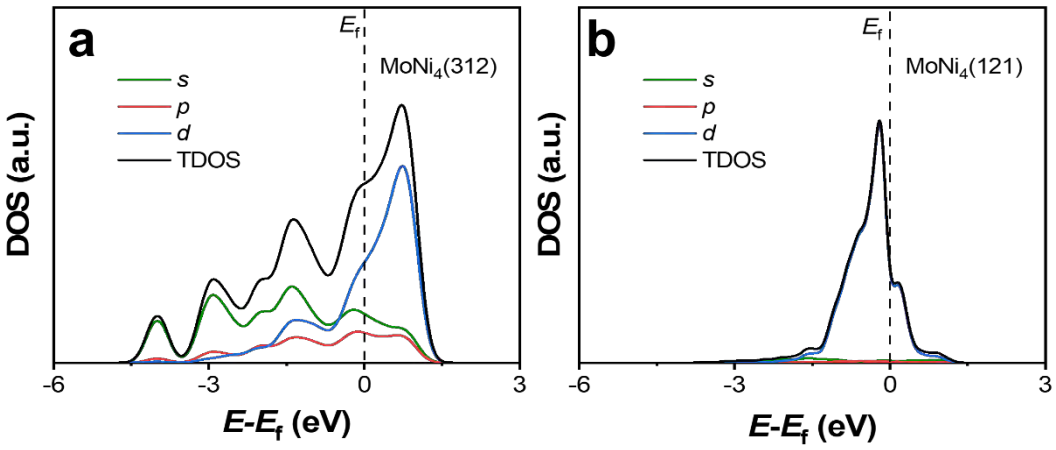

Figure S27. DOS of (a) MoNi4(312) and (b) MoNi4(121).

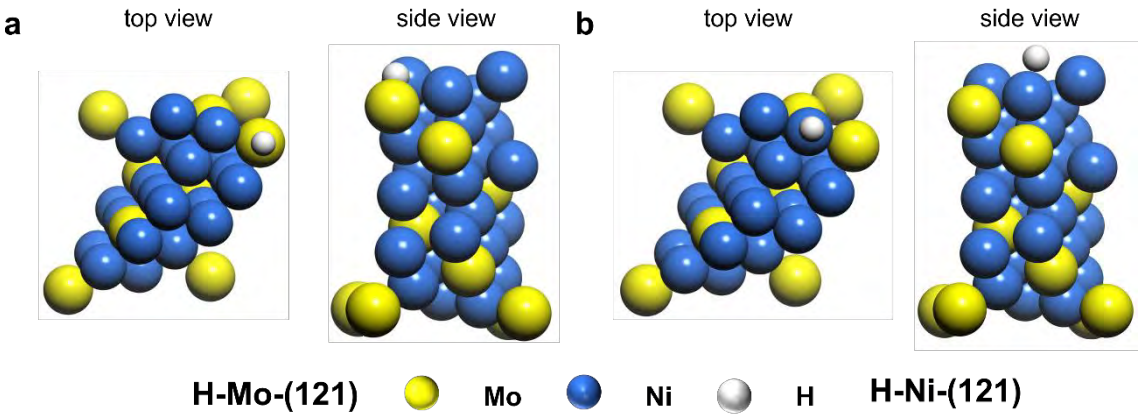

Figure S28. Model of H adsorption on (a) Mo and (b) Ni sites of $MoNi_4(121)$.

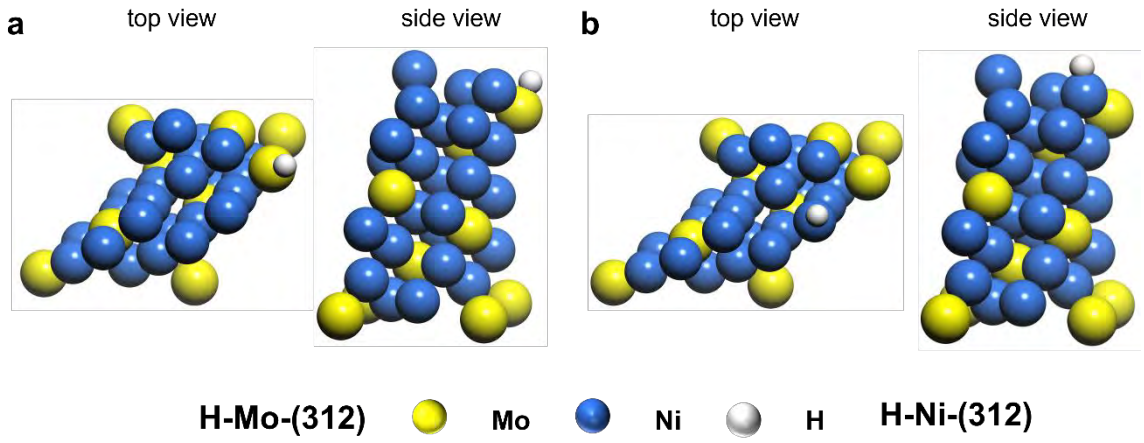

Figure S29. Model of H adsorption on (a) Mo and (b) Ni sites of $MoNi_4$(312).

References

[1] M. Zhang, D. Hu, Z. Xu, B. Liu, M. Boubeche, Z. Chen, Y. Wang, H. Luo, K. Yan, Facile synthesis of Ni-, Co-, Cu-metal organic frameworks electrocatalyst boosting for hydrogen evolution reaction, J. Mater. Sci. Technol., 72 (2021) 172-179.

[2] Z. Sun, L. Lin, M. Yuan, H. Yao, Y. Deng, B. Huang, H. Li, G. Sun, J. Zhu, Mott–Schottky heterostructure induce the interfacial electron redistribution of MoS_2 for boosting pH-universal hydrogen evolution with Pt-like activity, Nano Energy, 101 (2022) 107563.

[3] S. Sarwar, A. Ali, Y. Wang, M.R. Ahasan, R. Wang, A.J. Adamczyk, X. Zhang, Enhancement of hydrogen evolution reaction activity using metal–rich molybdenum sulfotelluride with graphene support: A combined experimental and computational study, Nano Energy, 90 (2021) 106599.

[4] H. Yang, P. Guo, R. Wang, Z. Chen, H. Xu, H. Pan, D. Sun, F. Fang, R. Wu, Sequential phase conversion-induced phosphides heteronanorod arrays for superior hydrogen evolution performance to Pt in wide pH media, Adv. Mater., 34 (2022) 2107548.

[5] Y. Zang, D.-Q. Lu, K. Wang, B. Li, P. Peng, Y.-Q. Lan, S.-Q. Zang, A pyrolysis-free Ni/Fe bimetallic electrocatalyst for overall water splitting, Nat. Commun., 14 (2023) 1792.

[6] I.H. Kwak, T.T. Debela, I.S. Kwon, J. Seo, S.J. Yoo, J.-G. Kim, J.-P. Ahn, J. Park, H.S. Kang, Anisotropic alloying of $Re_{1-x}Mo_xS_2$ nanosheets to boost the electrochemical hydrogen evolution reaction, J. Mater. Chem. A, 8 (2020) 25131-25141.

[7] A. Huang, H. Huang, F. Wang, N. Ke, C. Tan, L. Hao, X. Xu, Y. Xian, S. Agathopoulos, Mo_2C-based ceramic electrode with high stability and catalytic activity for hydrogen evolution reaction at high current density, Small, 20 (2024) 2308068.

[8] Y. Qian, J. Yu, Z. Lyu, Q. Zhang, T.H. Lee, H. Pang, D.J. Kang, Durable hierarchical phosphorus-doped biphase MoS2 electrocatalysts with enhanced H* adsorption, Carbon Energy, 6 (2024) e376.

[9] L. Du, D. Feng, X. Xing, C. Wang, G.S. Armatas, D. Yang, Uniform palladium-nickel nanowires arrays for stable hydrogen leakage detection and efficient hydrogen evolution reaction, Chem. Eng. J., 400 (2020) 125864.

[10] X. Bai, Q.-Q. Pang, X. Du, S.-S. Yi, S. Zhang, J. Qian, X.-Z. Yue, Z.-Y. Liu, Integrating RuNi alloy in S-doped defective carbon for efficient hydrogen evolution in both acidic and alkaline media, Chem. Eng. J., 417 (2021) 129319.

[11] D. Gao, J. Guo, H. He, P. Xiao, Y. Zhang, Geometric and electronic modulation of fcc NiCo alloy by Group-VI B metal doping to accelerate hydrogen evolution reaction in acidic and alkaline media, Chem. Eng. J., 430 (2022) 133110.

[12] M. Chen, Z. Liu, X. Zhang, A. Zhong, W. Qin, W. Liu, Y. Liu, In-situ phosphatizing of cobalt-molybdenum nanosheet arrays on self-supporting rGO/CNTs film as efficient electrocatalysts for hydrogen evolution reaction, Chem. Eng. J., 422 (2021) 130355.

[13] B. Liu, Y. Cheng, B. Cao, M. Hu, P. Jing, R. Gao, Y. Du, J. Zhang, J. Liu, Hybrid heterojunction of molybdenum disulfide/single cobalt atoms anchored nitrogen, sulfur-doped carbon nanotube /cobalt disulfide with multiple active sites for highly efficient hydrogen evolution, Appl. Catal. B-Environ., 298 (2021) 120630.

[14] J. Huang, Y. Liu, L. Wang, Z. Hou, Z. Zhang, X. Zhang, J. Liu, Coupling interactions enhancing molybdenum-based electrocatalysts for high-efficiency hydrogen evolution at wide pH, Chem. Eng. J., 469 (2023) 143908.

[15] J. Qu, Y. Li, F. Li, T. Li, X. Wang, Y. Yin, L. Ma, O.G. Schmidt, F. Zhu, Direct thermal enhancement of hydrogen evolution reaction of on-chip monolayer MoS_2, ACS Nano, 16 (2022) 2921-2927.